

**NASA Contractor Report 172420**

NASA-CR-172420  
19850002986

**Simulation Study of a New  
Inverse-Pinch High Coulomb  
Transfer Switch**

Sang H. Choi

Information & Control Systems, Incorporated  
Hampton, VA 23666

Contract NAS1-17488

October 1984

**LIBRARY COPY**

NOV 20 1984

LANGLEY RESEARCH CENTER  
LIBRARY, NASA  
HAMPTON, VIRGINIA

**NASA**

National Aeronautics and  
Space Administration

**Langley Research Center**  
Hampton, Virginia 23665

3 1176 00520 8856

---

ENTER:

1 RN/NASA-CR-172420

DISPLAY 07/6/1

85N11294\*\*# ISSUE 2 PAGE 194 CATEGORY 33 RPI#: NASA-CR-172420 NAS  
1.26:172420 FR-68#103 CNT#: NAS1-17488 84/10/00 71 PAGES

UNCLASSIFIED DOCUMENT

UTIL: Simulation study of a new inverse-pinch high Coulomb transfer switch  
ILSP: Final Report

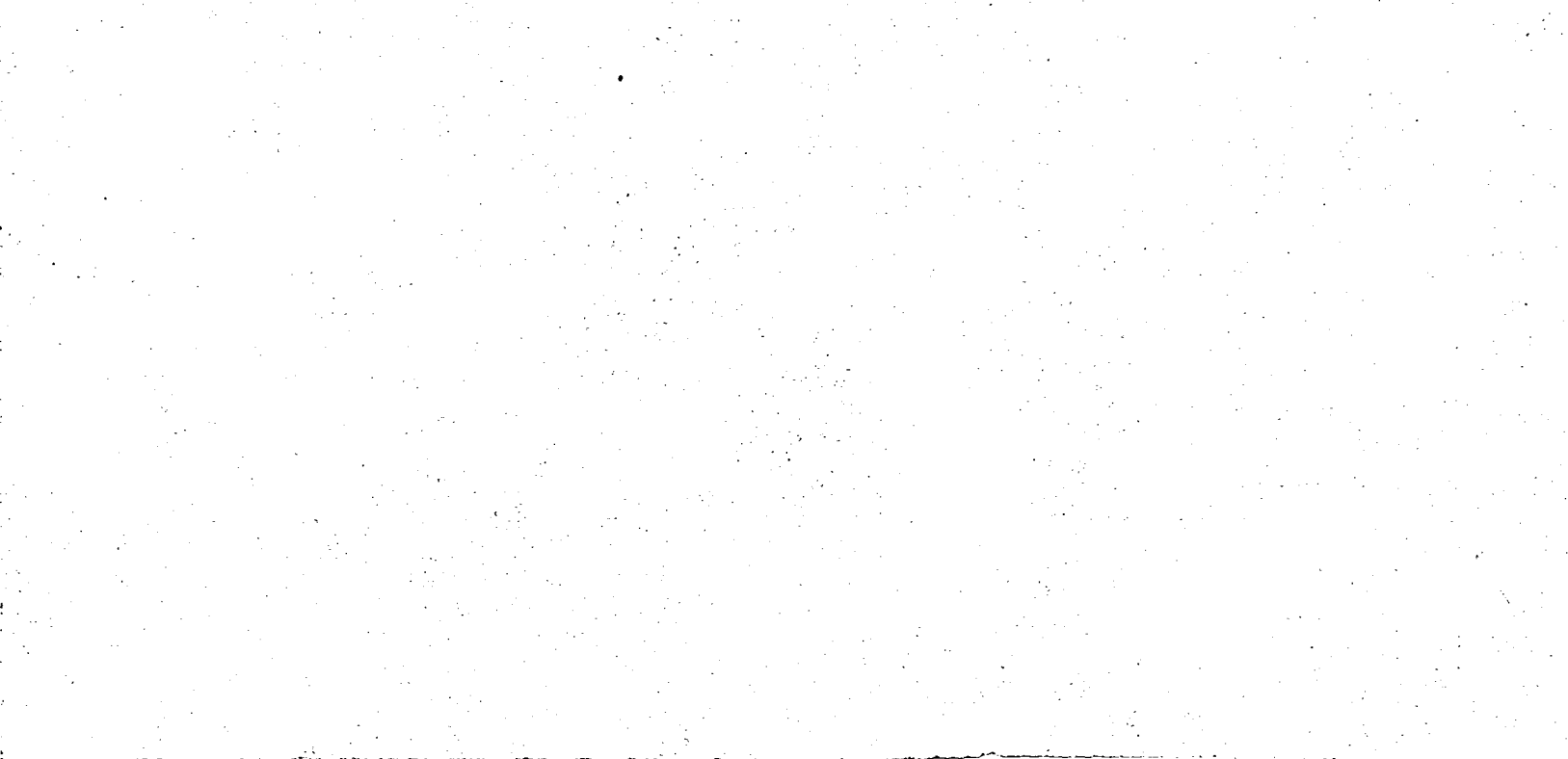
AUTH: A/CHOI, S. H.

CORP: Information and Control Systems, Inc., Hampton, Va. AVAIL.NIIS SAP:  
HC A04/MF A01

MAJS: /\*COMPUTERIZED SIMULATION/\*DESIGN ANALYSIS/\*MODELS/\*PARAMETER  
IDENTIFICATION/\*RELIABILITY/\*SWITCHES

MINS: / DAMAGE ASSESSMENT/ DATA CORRELATION/ ELECTRIC CURRENT/ ELECTRODES/  
PREDICTION ANALYSIS TECHNIQUES

ABA: M.A.C.



## ABSTRACT

A simulation study of a simplified model of a new and novel high-coulomb transfer switch has been performed. In contrast to the conventional trigger switch in which the currents are constricted by the z-pinch mechanism, the new switch operates in an inverse-pinch geometry formed by an all-metal chamber, greatly reducing hot-spot formations on the electrode surfaces. Advantages of the new switch over the conventional switches are longer useful life, higher current capability and lower inductance, which improves the characteristics required for a high repetition rate switch. The simulation study performed here determines the design parameters by analytical computations and comparison with the experimentally measured risetime, current handling capability, electrode damage, and hold-off voltages. Results from the simulation study show that the parameters of initial switch design can be determined for the anticipated switch performance. Results are in agreement with the experiment results. Although the model was simplified, it was accurate enough to determine the switch characteristics such as risetime, current handling capability, electrode damages, and hold-off voltages.



TABLE OF CONTENTS

	page
ABSTRACT . . . . .	i
LIST OF FIGURES. . . . .	iv
I. INTRODUCTION . . . . .	1
II. DESCRIPTION OF THE NEW SWITCH. . . . .	4
II-1. PRINCIPLE . . . . .	4
II-2. ADVANTAGES. . . . .	4
II-3. STATEMENT OF THE PROBLEM. . . . .	7
III. DESCRIPTION OF THE APPROACH. . . . .	10
IV. RESULTS AND DISCUSSIONS. . . . .	16
V. CONCLUSION . . . . .	20
REFERENCES . . . . .	48
APPENDIX A . . . . .	49

LIST OF FIGURES

	page
FIGURE 1. Z-PINCH MECHANISM AND ITS SWITCH CONFIGURATION. . . . .	3
FIGURE 2. INVERSE-PINCH MECHANISM AND ITS SWITCH CONFIGURATION. . . . .	5
FIGURE 3. CROSS-SECTION OF INVERSE-PINCH SWITCH AND SCHEMATIC . . . . .	6
FIGURE 4. EXTERNAL SWITCHING CIRCUIT DIAGRAM. . . . .	21
FIGURE 5. SIMULATION PROCEDURE FOR A HIGH POWER INVERSE-PINCH SWITCH. . . . .	22
FIGURE 6. FLOW CHART OF SWITCH COMPUTER SIMULATION MODEL. . . . .	23
FIGURE 7. CROSS-SECTION OF A NEW CLOSING INVERSE-PINCH. . . . .	24
FIGURE 8. CROSS-SECTION OF NEW CLOSING/OPENING SWITCH . . . . .	25
FIGURE 9. CURRENT SHEET LOCATION AT 3 SELECTED TIMES ALONG THE RADIAL DIRECTION. . . . .	26
FIGURE 10. CURRENT SHEET LOCATIONS AT 3 SELECTED TIMES. . . . .	27
FIGURE 11. CURRENT SHEET LOCATIONS AT 3 SELECTED TIMES. . . . .	28
FIGURE 12. DISCHARGE PLASMA CURRENT PROFILE DURING THE DISCHARGE PERIOD . . . . .	29
FIGURE 13. DISCHARGE PLASMA CURRENT CHANGES AT 3 SELECTED SYSTEMS INDUCTANCES. . . . .	30
FIGURE 14. AXIAL VELOCITIES OF CURRENT SHEET AT 5 DIFFERENT RADIAL POSITIONS. . . . .	31
FIGURE 15. AXIAL VELOCITIES AT 5 SELECTED RADIAL POSITIONS. . . . .	32
FIGURE 16. AXIAL VELOCITIES AT 5 SELECTED RADIAL POSITIONS. . . . .	33
FIGURE 17. RADIAL VELOCITIES OF CURRENT SHEET AT 5 DIFFERENT RADIAL POSITIONS. . . . .	34

LIST OF FIGURES (CONTINUED)

	page
FIGURE 18. RADIAL VELOCITIES AT 5 SELECTED RADIAL POSITIONS . . . . .	35
FIGURE 19. RADIAL VELOCITIES AT 5 SELECTED RADIAL POSITIONS . . . . .	36
FIGURE 20. AXIAL VELOCITIES AT 3 SELECTED DISCHARGE TIMES ALONG THE RADIAL DIRECTION . . . . .	37
FIGURE 21. AXIAL VELOCITIES AT 3 SELECTED TIMES ALONG THE RADIAL DIRECTION. . . . .	38
FIGURE 22. AXIAL VELOCITY PROFILES AT 3 SELECTED TIMES. . . . .	39
FIGURE 23. AXIAL VELOCITIES AT 3 SELECTED PRESSURES AND AT 0.8 $\mu$ sec .	40
FIGURE 24. AXIAL VELOCITY PROFILES BETWEEN ELECTRODES (1 and 13). . .	41
FIGURE 25. RADIAL VELOCITIES AT 3 SELECTED DISCHARGE TIMES ALONG THE RADIAL DIRECTION . . . . .	42
FIGURE 26. RADIAL VELOCITIES AT 3 SELECTED TIMES. . . . .	43
FIGURE 27. LEAK CURRENT AT 3 SELECTED PRESSURES DURING THE DISCHARGE PERIOD . . . . .	44
FIGURE 28. LEAK CURRENTS AT SELECTED SYSTEM INDUCTANCES . . . . .	45
FIGURE 29. DISCHARGE VOLTAGE VARIATIONS AT 3 SELECTED SYSTEM INDUCTANCES. . . . .	46
FIGURE 30. SWITCH INDUCTANCES AT 8 SELECTED PRESSURES . . . . .	47
FIGURE A. ASSEMBLY DRAWING. . . . .	51
FIGURE A-1. OBSERVATION VIEW WINDOW . . . . .	52
FIGURE A-2. ANODE ELECTRODE HEAD-DISK . . . . .	53
FIGURE A-3. SWITCH CHAMBER HOUSING (TOP). . . . .	54

LIST OF FIGURES (CONCLUDED)

	page
FIGURE A-4. HCP PLASMA TRIGGER INSULATOR. . . . .	55
FIGURE A-5. SWITCH CHAMBER HOUSING (BOTTOM) . . . . .	56
FIGURE A-6. CATHODE ELECTRODE . . . . .	57
FIGURE A-7. SWITCH SUPPORT SUBSTRATE. . . . .	58
FIGURE A-8. SWITCH INSULATOR BETWEEN ANODE AND CATHODE. . . . .	59
FIGURE A-9. ANODE ELECTRODE COLUMN. . . . .	60
FIGURE A-10. ANODE ELECTRODE CABLE CONNECTOR. . . . .	61
FIGURE A-11. ELECTRIC COAXIAL CABLE CONNECTOR FRAME . . . . .	62
FIGURE A-12. ASSEMBLY OF HCP PLASMA PUFF TRIGGER. . . . .	63
FIGURE A-13. CONNECTORS BETWEEN VIEW WINDOWS. . . . .	64

## I. INTRODUCTION

The development of an improved high-power, high-repetition-rate switch is essential for a number of applications, including excitation of pulsed high energy lasers, generation of energetic particle beams, magneto-plasma-dynamics (MPD) thrusters, inertial confinement fusion (ICF), and electric launchers (also called rail guns). Although various high power closing and opening switch concepts (1,2) have been studied, their performance demonstrated that the concepts still need improvements to overcome several significant state of the art limitations to high-power switching. These limitations include slow risetime (low  $dI/dt$ ), current handling capability, recovery time, thermal dissipation, irreversible switch damage, high-voltage hold-off, and various combinations of these. These are typical switch requirements found in special applications as mentioned above.

The most widely used high-coulomb transfer switches are trigatron spark gaps and thyratrons (3). Thyratrons have lower limits on voltage holdoff and current capability and therefore spark gaps are preferred over the limits of thyatron. The spark gaps suffer severe irreversible damage by hot-spot formations on the electrodes due to the z-pinch mechanism which constricts the current to an area of a few millimeters in diameter (4,5). Minor improvements of the geometry and/or adoption of special materials are insufficient to alleviate the effects of the z-pinch mechanism. The z-pinch mechanism results from the ponderomotive force  $\vec{F} = \vec{J} \times \vec{B}$  where  $\vec{J}$  is the current density, and  $\vec{B}$  the magnetic induction due to the current. (See Fig. 1).

In a recent development in a spark-gap switch, a laser beam was focused to trigger a spark between electrodes instead of using a trigger pin (2). Even though a laser triggered switch may have a much faster risetime than the conventional spark-gap trigatron, the electrodes' surface damage by hot-spot formation

due to the z-pinch mechanism is unavoidable. The consideration of fundamentally different approaches or ideas is accordingly important to overcome the state of the art limitations.

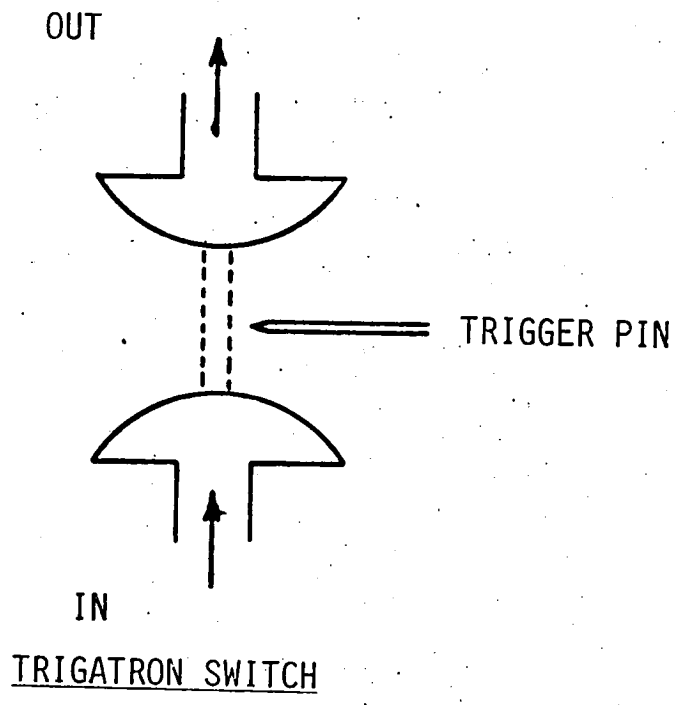
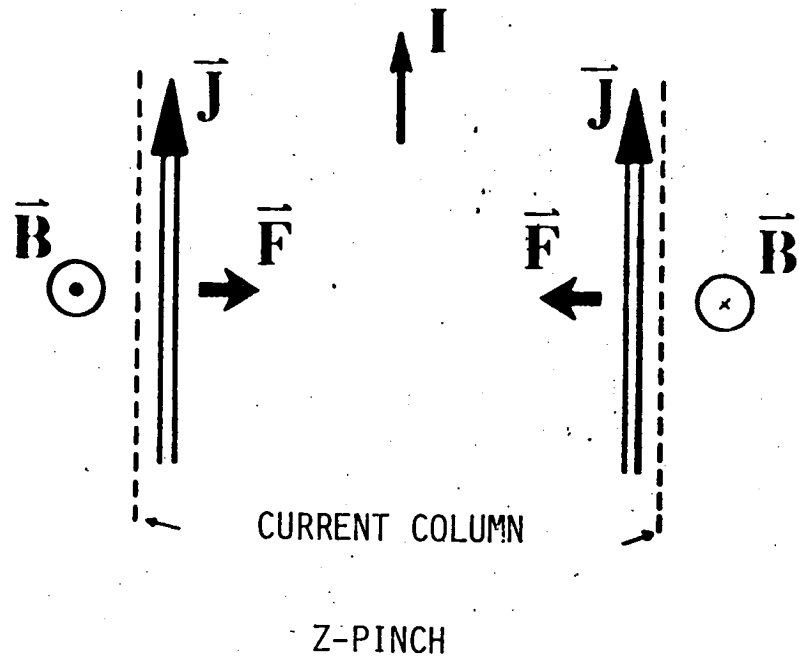


Figure 1. Z-pinch Mechanism and its switch configuration.

## II. DESCRIPTION OF THE NEW SWITCH

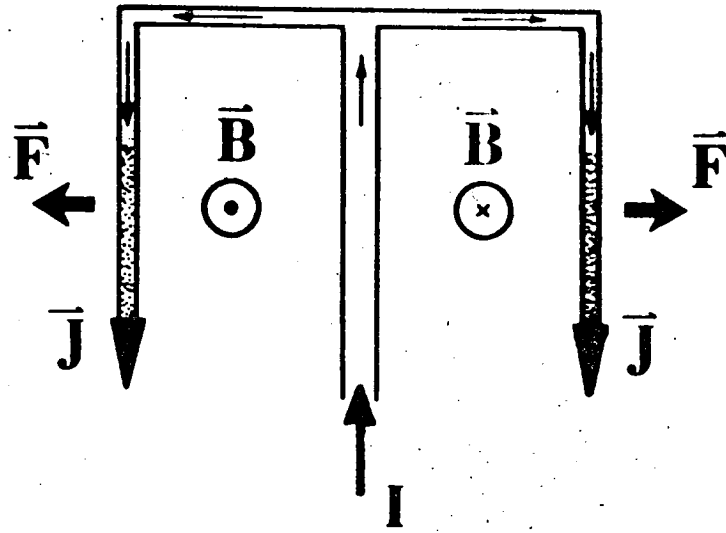
### II-1. PRINCIPLE

The new switch <sup>(6)</sup> described here has a novel geometry in which an inverse-pinch mechanism is operative and the ponderomotive force  $\vec{F} = \vec{J} \times \vec{B}$  is utilized to "disperse" and "move" the current sheet over the large area of the electrode surface instead of constricting the current. Figure 2 illustrates the inverse-pinch mechanism. Note that here the currents form the shape of a mushroom. This switch will be a "closing" switch, not primarily designed for "opening".

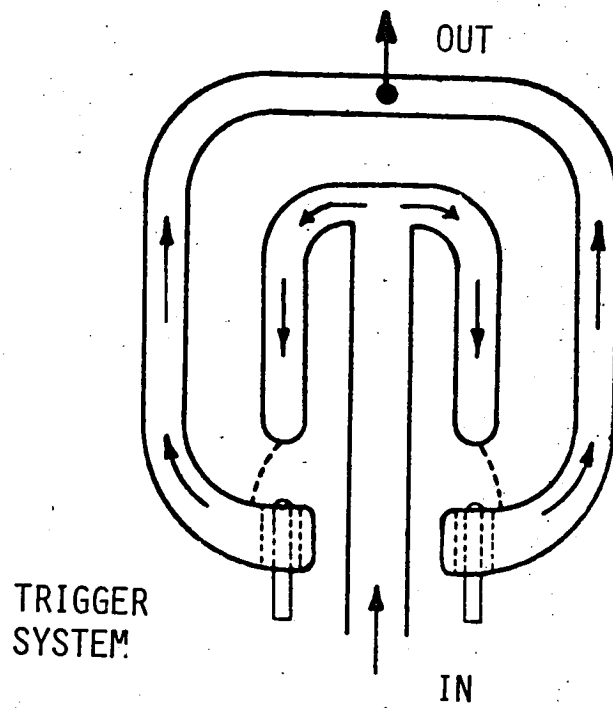
Figure 3 shows the cross section of the new switch. The inner, outer and return electrodes are cylindrical in general and are placed coaxially. The switching of the current takes place in the vacuum chamber formed by the inner and outer electrodes. The dotted lines indicate the currents at the time of the initial breakdown,  $I_o$ , at a later time (~1 micro-second),  $I_t$ , at the time of the peak current,  $I_p$ , and at the time when the current decreases near zero,  $I_f$ . The motion of the current sheet depicted here is the result of the inverse-pinch mechanism working on the plasma through which the current flows.

### II-2. ADVANTAGES

The following advantages over the conventional trigatron switches are recognizable from the description of the new switch above. (a) Reduced wear of the electrode material: This is expected from the fact that the strong pinch of the current sheet is eliminated from the new switch since the inverse-pinch mechanism is utilized for moving the "feet" of the current over a large area. (b) Reduced wear of the insulator material: For the same reason as above, fast detachment of the current sheet from the insulator shortens the period of exposure to the hot plasma and also alleviates a direct collision of ionized particles for the full discharge period. (c) Longer useful life: The advantages of (a) and (b) translate



INVERSE PINCH



INVERSE PINCH SWITCH

Figure 2. Inverse pinch mechanism and its switch configuration.

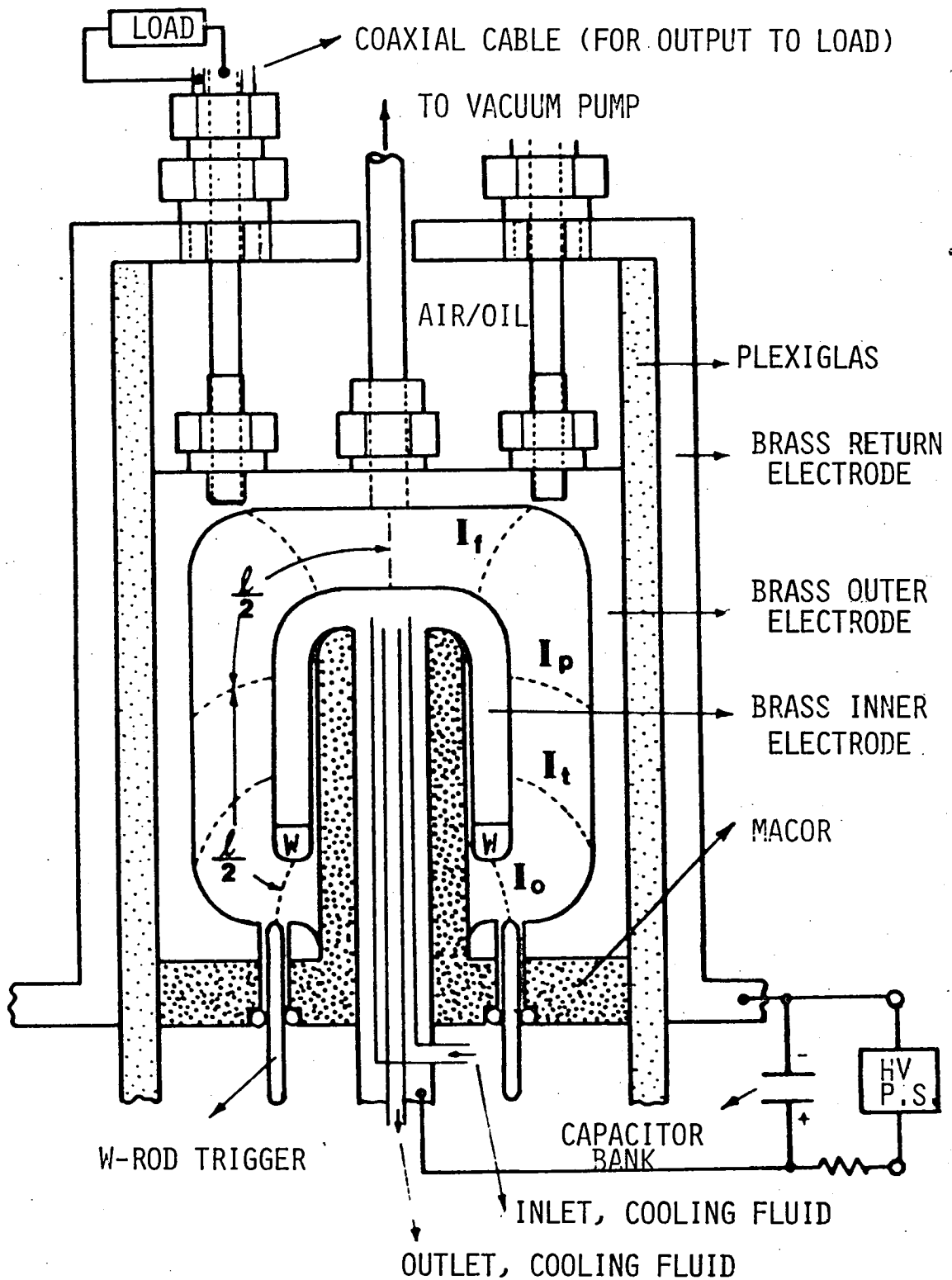


Figure 3. Cross section of inverse pinch switch and schematic.

into a longer useful life for the new switch in comparison with the conventional switches. (d) Higher current capability: The advantages of (a) and (b) also result in a higher current capability for the new switch in comparison with the conventional spark gaps. High power lasers applicable for welding, machining or laser weapons require switching of over 100 kA peak current at a repetition rate higher than 10Hz. Due to the reduced current density and rapid motion of the "feet" of the current on the electrode surface, a significant increase of the current capability for the new switch is expected. (e) Reduced switch inductance: The inductance of a unit length of a coaxial current sheet is expressed as  $(\mu/2) \ln(r_o/r_i)$  where  $\mu$  is permeability,  $r_o$  radius to the outer current, and  $r_i$  radius of the inner current. For the conventional trigatron, the ratio  $r_o/r_i$  becomes very large due to the reduction of  $r_i$  by z-pinch mechanism. For example,  $r_o = 10$  cm and  $r_i = .1$  cm or  $r_o/r_i = 100$  is typical for the conventional trigatron while  $r_o/r_i \leq 2$  is estimated for the new switch. A reduction of the inductance by a factor of  $\geq 7$  can be seen in this example. Since the risetime has the relation  $t_{1/2} = \frac{\pi}{2} \sqrt{LC}$ , a reduction of the component inductance is highly desirable for the fast pulsed power systems designed for laser excitation or generation of energetic particle beams.

### II-3. STATEMENT OF THE PROBLEM

The purpose of this study is to contribute to the development of an inverse-pinch switch which is predicted to operate beyond the present state of the art limitations. The results of preliminary experiments were reported by Choi and Lee (7). The preliminary experiments, which were a proof of principle, were performed at half atmospheric pressure of  $N_2$  gas in the switch chamber. The results from the tests were very promising. For instance, for a given 27 kilovolt trigger voltage and 10 kilovolt hold-off voltage, the current sheet formation was obvious

even though a limited number of trigger pins (4 pins in these tests) were used. The risetime measured by using a Rogowskii coil was less than or equal to  $1 \mu$  sec as predicted.

An effort to develop a switch beyond the state-of-the art limitations requires an analysis tool for better understanding of the switch performance and characteristics. The simulation model serves as an analysis tool which can be used to determine the problems and their solutions, to predict the switch performance, and to validate the parameters for a switch design. The performance analysis using the simulation model is desirable for a better understanding of the switch characteristics and its comparison with experimental work. The switch characteristics are related to the operational parameters such as the current distribution, the gap distance, the gas pressure, and the trigger mechanism for closing.

The simulation model can also predict the switch performance characteristics, such as: the wear pattern of electrodes and insulators (due to hot-spot formation on electrodes and long-standing exposure of insulators to the hot plasma); the risetime; the high current capability; the high voltage hold-off, and the recovery time. Therefore, the simulation model would also help estimate the useful life time of the switch.

The parameters, such as gap distance between electrodes, gas pressure, trigger mechanism, and current-sheet behavior, useful for the prototype switch design may be obtained by correlating the input parameters and output results. This approach is an effective and economic way to assess the feasibility of a new switch for high-power scaling. The design parameters can also be determined by experimental results. However, in most cases an experiment turns out to be a time-consuming and costly approach.

The current simulation model is limited to a simplified version and uses

the continuity, momentum, and magnetic field equations for the plasma motion with appropriate initial conditions (ICs) and boundary conditions (BCs) for the geometry of the inverse-pinch switch shown in Fig. 3. If coupled to the equation of the switching circuit (see Fig. 4), the model can be used for the analysis of major phenomena while the switch is closing.

Among the major phenomena which appear while switching are the current sheet formation at a particular time and its motion. These are the key factors that determine directly or indirectly the wear patterns of electrodes and insulators, the current capability, the risetime and eventually the useful life of a switch.

The simplified model serves to determine a few important parameters such as current sheet formation and motion during switch operation. However, it lacks the capability to characterize the switch operation with respect to the input and plasma parameters (see Fig. 5). Accordingly, for detailed understandings of the switch performance, a full scale 2-dimensional simulation model is being developed using the alternating direction implicit (ADI) finite difference scheme which is a powerful numerical method.

The full-scale model consisting of the mathematical model and simulation software will serve as a tool for diagnostics and performance analysis, and as a method for a parameter estimation for the design of a prototype switch. This approach is necessary for developing an improved high-power, high rep-rate switch. Therefore, the efforts in developing the model should be carried out in parallel with the progress of the switch design.

Further applications of the simulation model are possible since the coding is general and complete. For instance, with a slight modification to the model, it can be used for the analysis of various plasma devices, such as plasma light sources for laser pumping, and dense plasma production systems (i.e., hypocycloidal pinch (HCP) and z-pinch apparatus).

### III. DESCRIPTION OF THE APPROACH

The frame of the simulation software system was initiated with a complete set of plasma fluid model (MHD) equations. This set of equations satisfies given spatial and temporal domains which are continuous and bounded. When the domain of switching action is defined (for example, Figs. 3, 7, and 8) the initial and boundary conditions can be identified by switch operation and configuration, respectively. In other words, the initial conditions are determined by the input power, external electric circuit, the boundary conditions by the switch configuration, and prescribed conditions (such as flow field, thermal field, and magnetic field). Such equations with ICs and BCs can then be used as a mathematical model when certain assumptions are made because of geometrical symmetry, negligible quantity of a certain model property, computational difficulty, and negligible effects of a certain physical phenomenon.

The MHD equations were set up for the mathematical model with an axial symmetric condition (2-dimensional). Subsequently the mathematical model was written into numerical form using the alternating direction implicit (ADI) finite difference scheme and coded.

A simplified version of the code was derived by considering the external electrical load circuit and the momentum equations. This simplified model has a capability to compute the motion of the current sheet due to the ponderomotive force, the velocity profiles, the current capability, and the inductance.

An understanding of the mechanism of current-sheet formation and the current variation along the axial and radial directions with respect to time is absolutely necessary for the analysis of switch performance. The results of the study, together with the solution to an external circuit equation using time dependent plasma inductance and electrical parameters of the circuit, will determine not only the risetime, but also the total current flowing at a particular time.

The current-sheet activities will also help determine the loci of the damage on electrode surface along the axial direction and thereafter the thermal dissipation from the hot-spot.

There are three regimes of switch operation: 1) closure, or initiation of the switch conductive phase; 2) conduction or rundown phase; and 3) recovery, or opening phase. The second (conduction) phase that occurs along the annular portion (the Mather geometry) becomes an important part because its results would show a picture of the current sheet formation and motion and the total current flowing as a time dependent function. This analysis is somewhat similar to a plasma focus problem (8).

The closure phase plays an important role in determining the risetime, and the jitter effects. The trigger pins or laser trigger form a non-uniform azimuthal distribution of the initial arc or spark between triggers until plasma growth is fully achieved. In this case, the geometry involved in the analysis would be spherical coordinates (3 dimensional) as opposed to the cylindrical coordinates (2 dimensional) in the second (conduction) phase. Due to the geometry, non-uniformity of a plasma, jitter, and etc., the first phase for closure is a complicated problem. Hence, none of the analysis has been done in this area.

The third phase, or opening, takes place when the current sheet is focused and constricted due to z-pinch mechanism on the top of the inner electrode shown in Fig. 3. To avoid the dense plasma focus on the top of the inner electrode, the opening phase for the purpose of a closing switch is designed to carry a diminishing current after the peak current. Hence, the spot damage on the electrode is avoided or alleviated. An opening switch version which uses the principle of  $m=0$  instability to cut off the current during the plasma focus is shown in Fig. 6. This opening switch has only a slightly different

configuration to the inner electrode than that shown in Fig. 3. Therefore, this inverse-pinch closing switch can be easily converted into the opening switch by a minor design change of the electrode. One possible geometry is shown in Fig. 6.

The analysis of the third phase will determine the recovery time. However, as in the first phase, the third phase poses as a complicated problem which has not similarity with the second phase. Hence, the problem must be treated with boundary conditions which are related to the Z-pinch mechanism and coupled with the second phase. The results of the second phase could be used as the initial conditions to the third phase.

The following MHD equations are the expressions that were used for the mathematical model of the inverse-pinch high-power switch:

The continuity equation:

$$\frac{\partial \rho}{\partial t} + \nabla \cdot (\rho \mathbf{V}) = 0 \quad (1)$$

The momentum equation:

$$\rho \frac{\partial \mathbf{V}}{\partial t} + \rho (\mathbf{V} \cdot \nabla) \mathbf{V} + \nabla [n (k T_e + k T_i)] = \frac{1}{c} (\mathbf{J} \times \mathbf{B}) - \nabla \cdot \pi \quad (2)$$

The energy equation for ions:

$$\begin{aligned} \frac{k}{\gamma-1} \frac{\partial}{\partial t} (n T_i) + \frac{k}{\gamma-1} \nabla \cdot (n T_i \mathbf{V}) + k n T_i (\nabla \cdot \mathbf{V}) + \pi_{\alpha\beta} \frac{\partial V_\alpha}{\partial X_\beta} + \nabla \cdot \mathbf{q}_i \\ = Q_i + \frac{\xi}{2} [\mathbf{J} \cdot \nabla T_i + p \nabla \cdot \left( \frac{\mathbf{J}}{\rho} \right)] \end{aligned} \quad (3)$$

The energy equation for electrons:

$$\frac{k}{\gamma-1} \frac{\partial}{\partial t} (n T_e) + \frac{k}{\gamma-1} \nabla \cdot (n T_e \mathbf{V}) + k n T_e (\nabla \cdot \mathbf{V}) + \nabla \cdot \mathbf{q}_e = -Q_i + \eta J^2 + W_{ei} \quad (4)$$

The magnetic field equation:

$$\frac{\partial H}{\partial t} = \nabla_x(V_x H) - \nabla_x(\nu J) - \frac{\xi}{2} \nabla_x \left( \frac{J_x H - \frac{1}{2} \nabla P}{\rho} \right) \quad (5)$$

The above equations are theoretically well defined and can be found in almost every plasma physics book. Therefore, further explanation about the terms in the equations is omitted here for brevity.

Equations 1-5 in their applications to the switching domain are integrated with the external electric circuit equations. The electric circuit equations were developed based on a standard circuit for a switched power supply (see Fig. 4). The terminal voltage drop ( $V_c$ ) at capacitor is

$$V_c = R_E I + L_E \frac{dI}{dt} + L_s \frac{dI_p}{dt} + L_p \frac{dI_p}{dt} + R_p I_p \quad (6)$$

and the terminal voltages for the leak and plasma current during switching are the same. Thus

$$R_L I_L + L_L \frac{dI_L}{dt} = (L_s + L_p) \frac{dI_p}{dt} + R_p I_p \quad (7)$$

The total circuit current is

$$I = I_L + I_p = \frac{dV_c}{dt} \quad (8)$$

There is another equation (9) that expresses the rate of change of the plasma inductance. The plasma inductance ( $L_p$ ) varies with respect to time,

$$\frac{dL_p}{dt} = 2 \times 10^{-9} \left[ V_z \ln \frac{R_o}{r} + V_z \frac{r z t}{R_o^2} + \frac{z V_r}{r} \right] \quad (9)$$

where the subscripts o, r, t, z denote the outside diameter, r-direction, bottom tip of a node, and z-direction, respectively.

When the above 9 equations are transformed into numerical equations by employing ADI scheme, the number of equations increases to 14. The solutions to the 14 numerical equations require the inverse of tri-diagonal matrices which can be done by the TRI-DIAGONAL routine more efficiently and faster than the conventional matrix inversion. As a whole, the ADI scheme and TRI-DIAGONAL routine will be the main routines for handling the model equations with reasonable accuracy and stability.

The general expressions of the plasma parameters were already included in Eqs. 1-5. These parameters are the ion viscosity tensor, ( $\pi$  in Eqs. 2 and 3), the conduction loss of ions ( $q_i$  in Eq. 3), the conduction loss of electrons ( $q_e$  in Eq. 4), the Hall effects (the last terms of Eqs. 3 and 5), the ion energy change due to electron-ion collisions ( $Q_i$  in Eqs. 3 and 4), the Joule heating ( $\eta$  in Eq. 4), the Bremsstrahlung ( $W_{e-i}$  in Eq. 4), the electron density ( $n$  in Eqs. 2, 3 and 4), the magnetic viscosity ( $\nu$  in Eq. 5), and the Coulomb logarithm.

The precise expressions of plasma behavior and switch performance are essential to analyze the switch characteristics, and to define and identify the input and output parameters for the prediction and estimation for the switch design. To obtain the precise expressions of plasma behavior and switch performance, the integration of important plasma parameters into the mathematical model is required. However, in the simplified model, these parameters are ignored because of the difficulty of computation or in some cases they have a negligible effect.

Since the momentum equation can approximately describe the current formation and motion, the energy equations for electron and ion were omitted in the simplified model. Accordingly, the simplified model consists of two momentum equations for axial and radial flow, and four (Eqs. 6, 7, 8 and 9) for external electrical load circuit.

Rewriting Eq. 2 for the radial and axial direction variations of the current sheet due to the ponderomotive force, we have

$$\rho \frac{\partial u}{\partial t} + \rho v \frac{\partial u}{\partial r} + \rho u \frac{\partial u}{\partial z} = -J_z B_\theta \quad (10)$$

for the momentum equation in the radial direction, and

$$\rho \frac{\partial v}{\partial t} + \rho v \frac{\partial v}{\partial r} + \rho v \frac{\partial v}{\partial z} = J_r B_\theta \quad (11)$$

for the momentum equation in the axial direction.

First, for defining the plasma inductance Eq. 9 is solved with the initial velocities. Then Eqs. 6, 7 and 8 with the plasma inductance (which was obtained from Eq. 9) are solved to determine the switch current, leak current, and terminal voltage drop at capacitor. The results from Eqs. 6, 7 and 8 are then used in Eqs. 10 and 11. In Eqs. 10 and 11 the current densities ( $J_z$  and  $J_r$ ) are represented by the induced magnetic field ( $J = \nabla \times H$ ). Accordingly, the switch current is used to compute the induced field strength in the switch chamber. At each time step, loci of the current sheet front are determined by the velocities obtained from Eqs. 10 and 11, and at the same time the plasma inductance is determined and used as input data in the external circuit Eqs. 6, 7 and 8. The new switch current is then located on the front of the current sheet and used to determine the velocities and subsequent current sheet front.

#### IV. RESULTS AND DISCUSSIONS

In the simplified model the input parameters such as inductances, resistances, and capacitance of the external circuit (Fig. 4) and switch configuration (Fig. 3) were selected based on the experiment performed earlier (7). The parameters for external electric circuit are the followings:

Capacitor charge	$20 \times 10^{-6}$	Farad
Hold-off Voltage	15	kV
Switch Inductance	$41 \times 10^{-9}$	Henry
System Inductance	$700 \times 10^{-9}$	Henry
System Resistance	1.0	ohm
Leak Circuit Resistance	5.0	ohm

The switch geometry are the followings:

Radius of Inner Electrode (Anode):	0.0365	m
Radius of Outer Electrode (Cathode):	0.0643	m
Length of Inner Electrode:	0.2081	m
Length of Outer Electrode:	0.235	m

And others are:

Gas Pressure:	7	mTorr
Gas Density:	$5.84 \times 10^{-6}$	kg/m <sup>3</sup>

With the above parameters the simulation procedure was set up to test the switch characteristics by varying the system inductance and the gas pressure. The system inductances selected here for the test are 100 nH, 400 nH, and 700 nH, and the gas pressures are 0.7 mTorr, 4.3 mTorr, and 8 mTorr. The system inductance determines the risetime. The risetime and the current sheet velocity eventually determine the loci of peak current on the electrode. Furthermore, the inductance and current flow pattern determine the exposure period and the wear of the electrodes and insulator. The gas pressure is a factor that

also determines a hold-off voltage, plasma motion and traveling distance of plasma which will eventually determine the switch size. At relatively high gas pressure, the distance the current sheet travels becomes short, so that the discharge takes place over a limited area of the electrodes. In the case of high pressure and high current flow the damage on the electrodes would be inevitable even though the inverse-pinch is operative. However, the situation is still better when compared to the z-pinch mechanism.

The results obtained from the simplified model by manipulating the previous two parameters, the system inductance and the gas pressure, are shown in Figs. 9-32. Several parameters were also selected and are plotted which describes the switch performance.

Figures 9, 10, and 11 show that the loci of the current sheet vary with the gas pressure in the switch chamber and with the system inductance. In Fig. 9 the location of the current sheet was calculated along the radial direction between the electrodes while the gas pressure ( $p$ ) was maintained at 0.7 mTorr and the system inductance ( $L_{\text{sys}}$ ) at 100 nH. In Fig. 10, the pressure was at 8 mTorr with the same system inductance as in Fig. 9. The density or pressure in the switch chamber dramatically controls the current sheet motion. At a system inductance of  $L_{\text{sys}} = 100$  nH the risetime was approximately 0.8  $\mu\text{sec}$  as shown in Fig. 12. During the risetime the progress of the current sheet was limited to about 6 cm from the bottom of the switch for a gas pressure  $p = 0.7$  mTorr (see Fig. 9) and to about 2 cm from the bottom of the switch when the gas pressure was 8 mTorr. When the energy equation was included to take the shock front into account, the real front of the current sheet would be slight above the location of the current sheet calculated from the simplified model. Figure 11 shows the location of the current sheet when the system inductance was  $L_{\text{sys}} = 700$  nH. In this case the risetime is about

3  $\mu$ sec as shown in Fig. 13. Accordingly, the location of the peak current flow can be seen at about 22 cm from the bottom of the switch. However, the length of the actual anode is 20.81 cm so that the peak current occurs in the region of the z-pinch phenomena on the top of the anode electrode.

Figures 12 and 13 show that the discharge switch current varies with the system inductance rather than the effects from pressure changes. The chamber gas pressure has a great influence on the discharge plasma inductance. However, the effects on the discharge current from the gas pressure are not visible in Fig. 12 because the discharge inductance is negligibly small compared to the system inductance.

Figures 14, 15 and 16 show the axial velocity variations at 5 selected radial positions during the discharge period. The velocity variation in Fig. 14 was obtained at the gas pressure  $p = 0.7$  mTorr and the system inductance was  $L_{\text{sys}} = 100$  nH. In Fig. 15, the gas pressures were 8 mTorr. The differences shown in Fig. 14 and 15 were due to the gas pressure. In Fig. 16 the pressure was 0.7 mTorr and the system inductance was 700 nH. As illustrated in Figs. 14, 15, 16, 17, 18 and 19 the pattern of velocity variations resembles the discharge current variation which is determined predominantly by the system inductance. Figures 17, 18 and 19 show the variations of radial velocity during the discharge period. Figure 13 shows that by reducing the system inductance the risetime can be shortened by a noticeable amount.

Figures 20, 21, 22 show the axial velocity distributions along the radial direction at 3 selected time. The axial and radial velocities are determined predominantly by the system inductance, the discharge current, and the gas pressure in the switch chamber. Figure 23 shows the axial velocity distributions as a function of gas pressure. Figure 24 shows the axial velocity as a function of the system inductance. In the same way Figs. 25 and 26 show the radial velocity distributions along the radial direction.

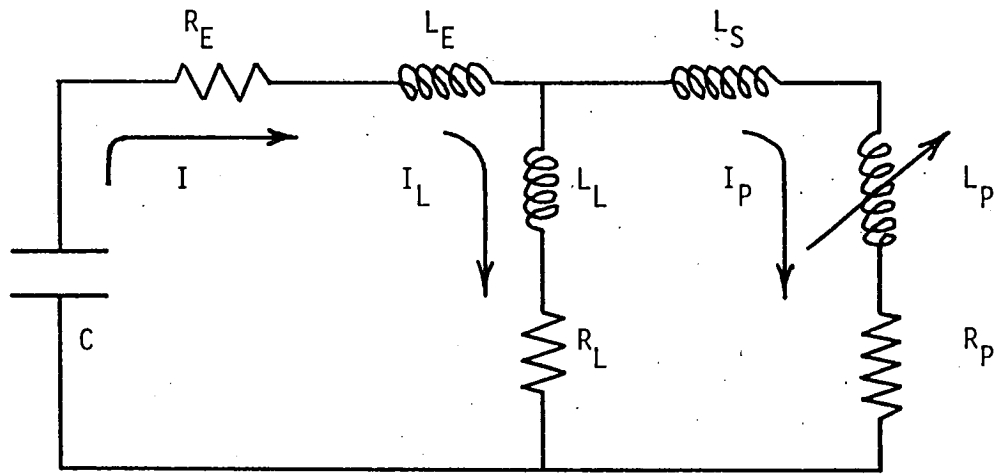
Figures 27 and 28 illustrate the variations of leakage current. Figure 26 shows that the leakage current is little affected by the change of gas pressure. However, the system inductance has an influence on the leakage current as shown in Fig. 28. In this case a leakage resistance of 5 ohms was used. Figure 29 illustrates the discharge voltage variations with respect to the system inductances during the discharge period. Figure 30 shows the variation of plasma inductance at variable gas pressure during the discharge period. Although the plasma inductances are increased due to the motion of the current sheet, the plasma inductance is several orders of magnitude less than the system inductance. Hence, to achieve a fast risetime while switching, an effort to decrease the system inductance must first be made.

## V. CONCLUSION

Even when a simplified model is used to simulate the inverse-pinch switch shown in Fig. 3, the results clearly show that the simplified simulation model performs well enough to describe switch performance and characteristics. The results shown in the figures compare well with results from the experiment <sup>(7)</sup>. For instance, in the experiment the risetime with a system inductance of 700 nH and a gas pressure of 0.7 mTorr was observed to be about 3  $\mu$ sec, which is very close to the result of the calculation ( $\sim 2.75 \mu$ sec) shown in Fig. 13.

As discussed in the section IV, the inverse-pinch switch mechanism is consistent with the simulation study and the results of experiment. The results also show that the inverse-pinch switch can overcome the state of the art limitations, by its advantages such as reduced wear of electrodes and insulator, fast risetime, high current capability, and consequently a longer useful life.

A new inverse-pinch switch was designed and built during the period of the contract. This new switch is currently installed and being tested in the laboratory. The detailed design of the switch is illustrated in the assembly and parts drawings which are attached in Appendix A.



- C - EXTERNAL CAPACITANCE
- $R_E$  - EXTERNAL RESISTANCE
- $L_E$  - EXTERNAL INDUCTANCE
- $L_L$  - LEAK INDUCTANCE
- $R_L$  - LEAK CURRENT RESISTANCE
- $L_S$  - SWITCH INDUCTANCE
- $L_P$  - PLASMA INDUCTANCE
- I - TOTAL CIRCUIT CURRENT
- $I_L$  - LEAK CURRENT
- $I_P$  - PLASMA CURRENT

Figure 4. External Switching Circuit Diagram.

REQUIREMENTS FOR A HIGH POWER SWITCH:

- a. FAST RISE TIME
- b. HIGH CURRENT CAPABILITY
- c. HIGH REPETITION RATE
- d. LOW WEAR OF ELECTRODE & INSULATORS  
(LONG LIFE)

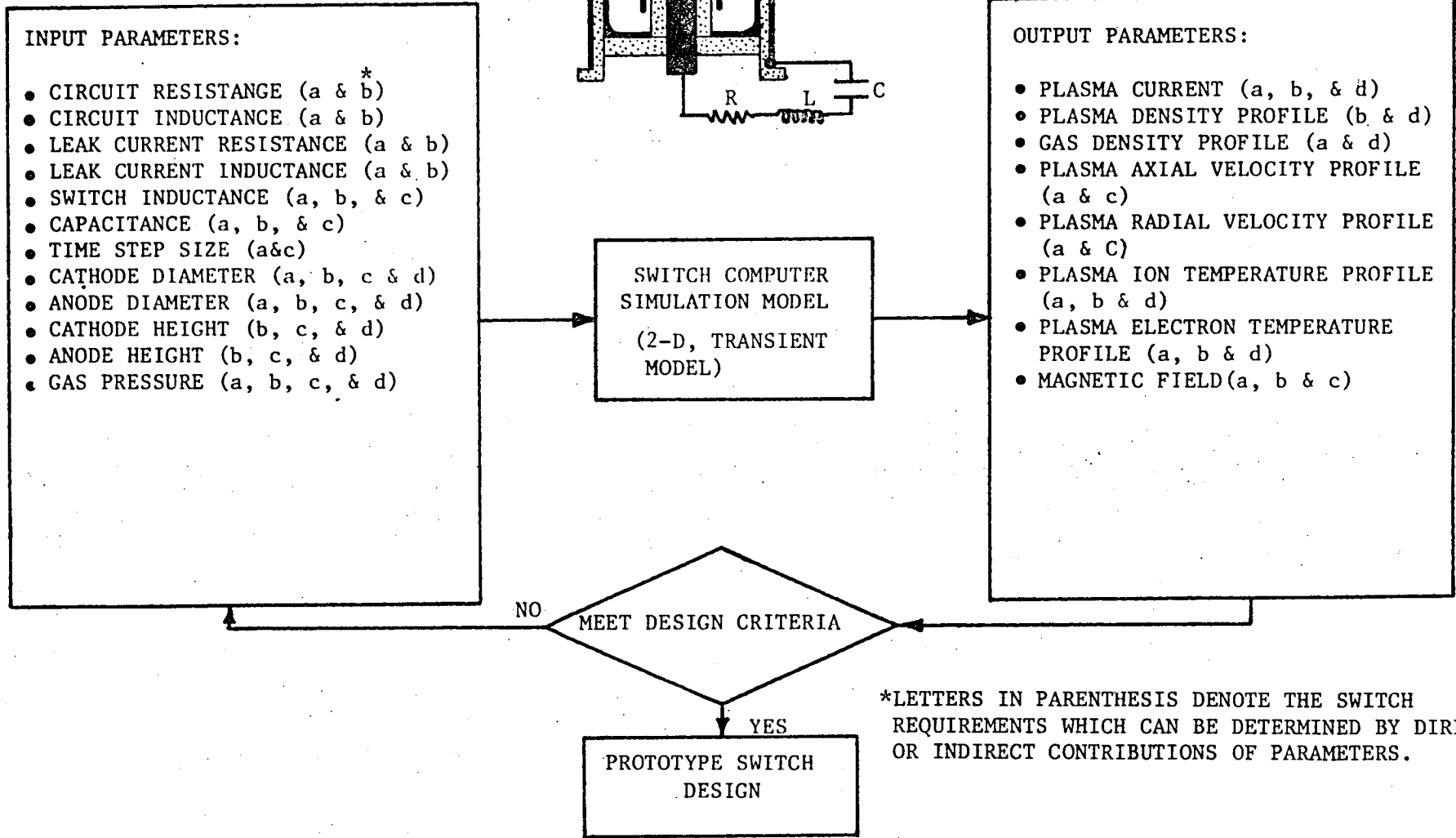
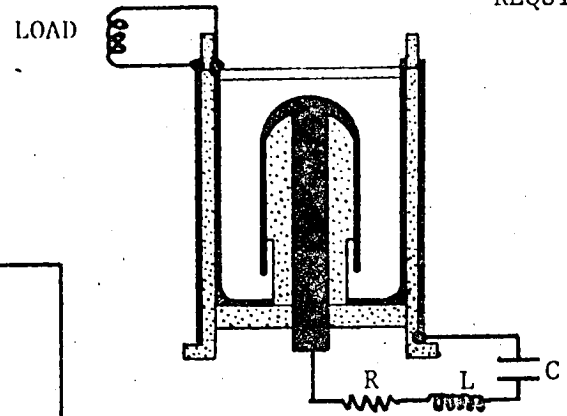
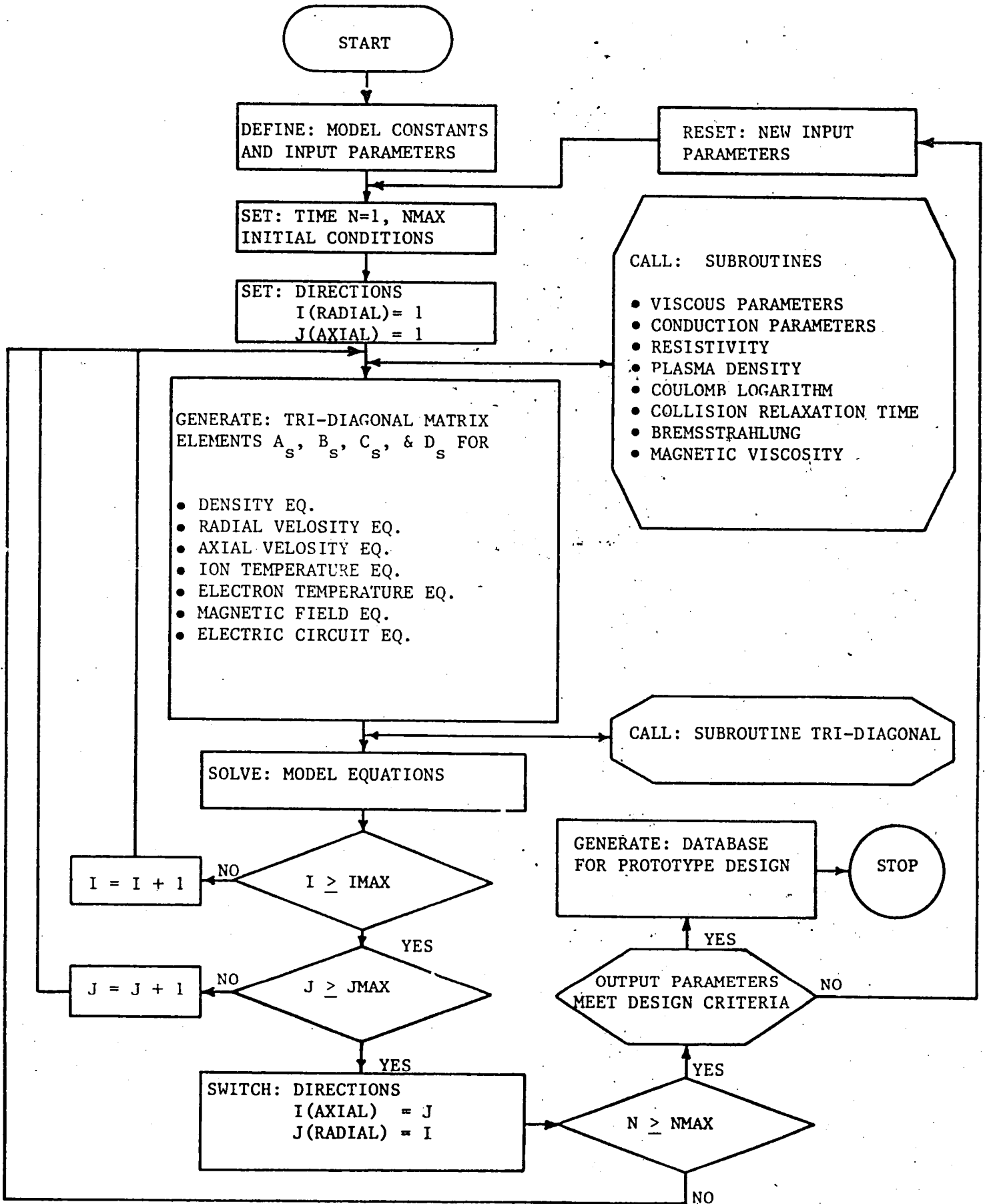


Figure 5. Simulation Procedure for a High Power Inverse-Pinch Switch

Figure 6. Switch Computer Simulation Model Flow Chart.



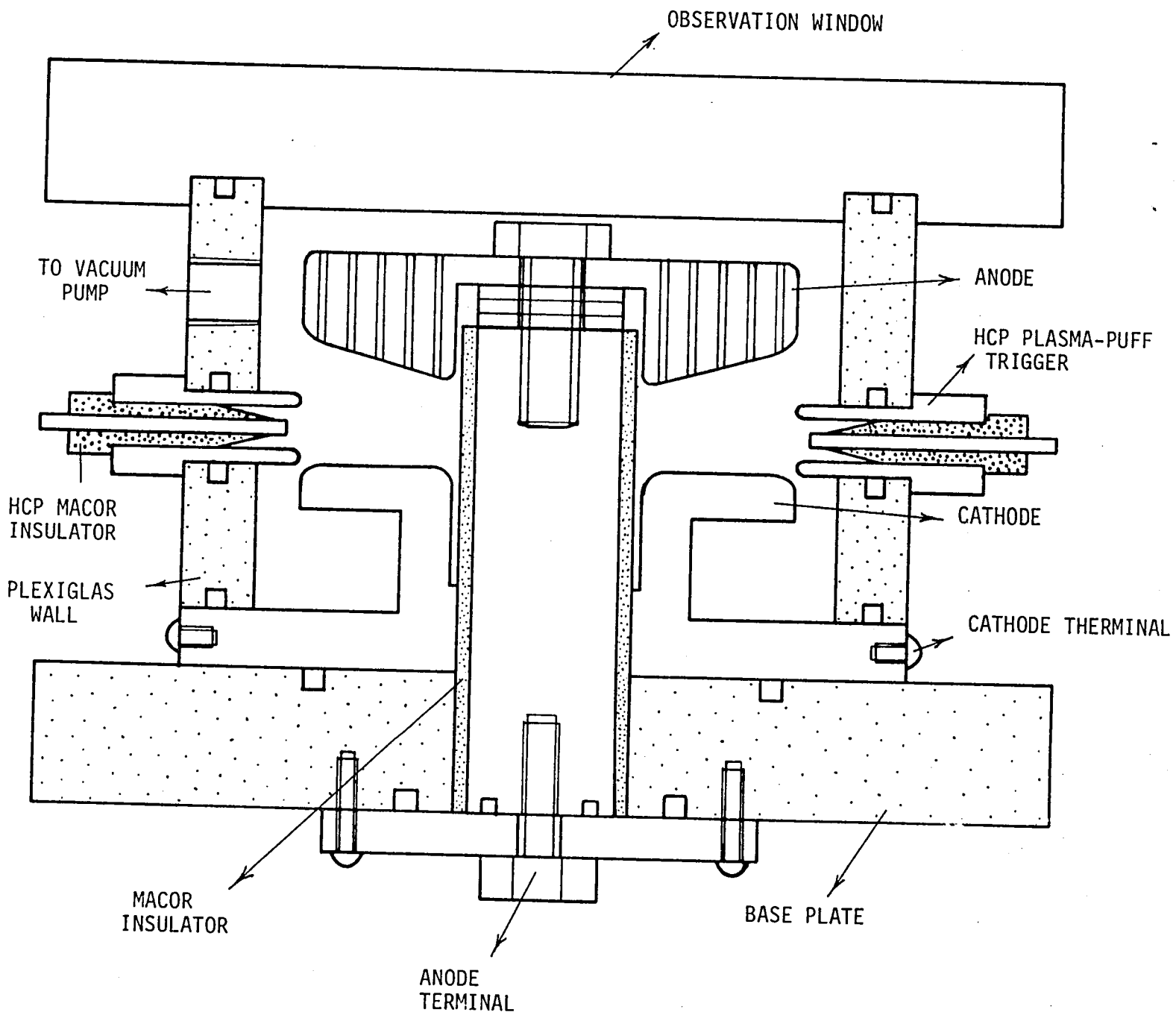


Figure 7. Cross-Section of a New Closing Inverse-Pinch Switch.

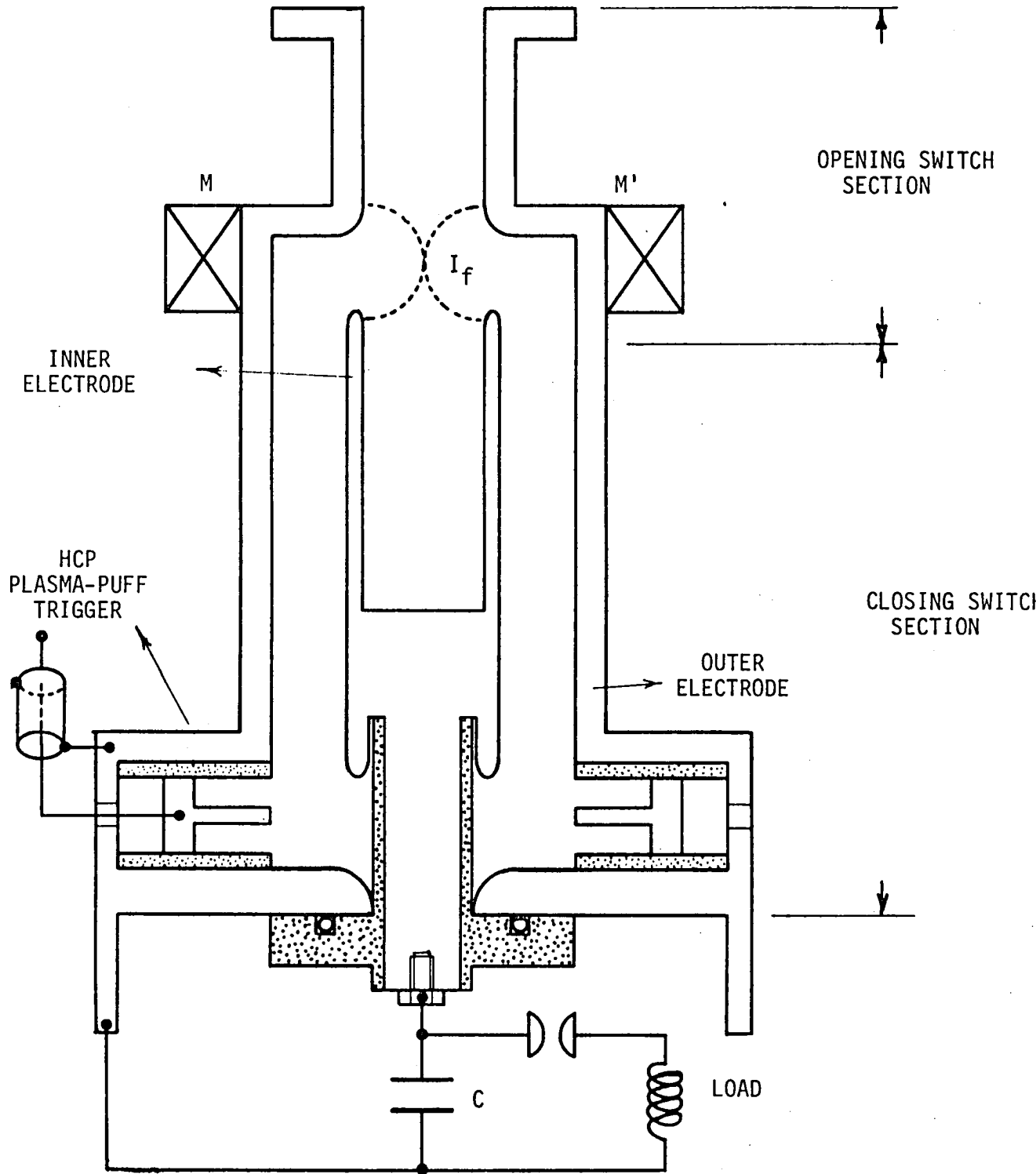


Figure 8. Cross-section of new Closing/Opening switch. The bottom portion of the C/O switch consist of the inner and outer electrodes and HCP plasma-puff trigger mechanism for the closing phase. The top portion of the C/O switch consist of the inner and outer electrodes and magnet for the pinch of plasma current. The opening switch uses  $m=0$  instability to cut off the plasma current.

\_\_\_\_\_ TIME = .1  $\mu$ sec  
 - - - - - TIME = .8  $\mu$ sec  
 \_\_\_\_\_ TIME = 3.1  $\mu$ sec

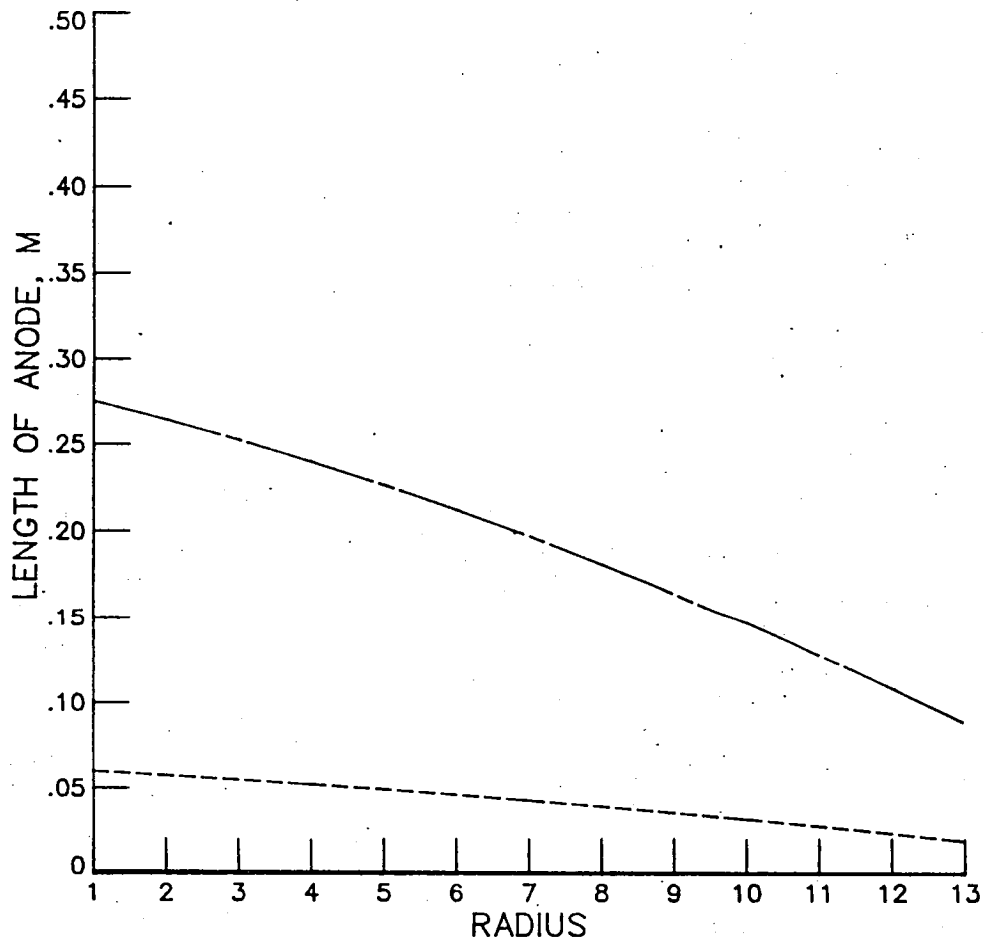


Figure 9. Current sheet location along the radius at three selected times. The number 1 ( $r_i = 0.0365$  m) corresponds to the inner electrode (anode) and 13 ( $r_o = 0.0643$  m) corresponds to the outer electrode (cathode). The gas pressure was 0.7 mTorr and the system inductance was 100 nH. The current sheet at 0.1  $\mu$ sec almost remains on the initial location.

—————	TIME =	.1 $\mu$ sec
- - - - -	TIME =	.8 $\mu$ sec
—————	TIME =	3.1 $\mu$ sec

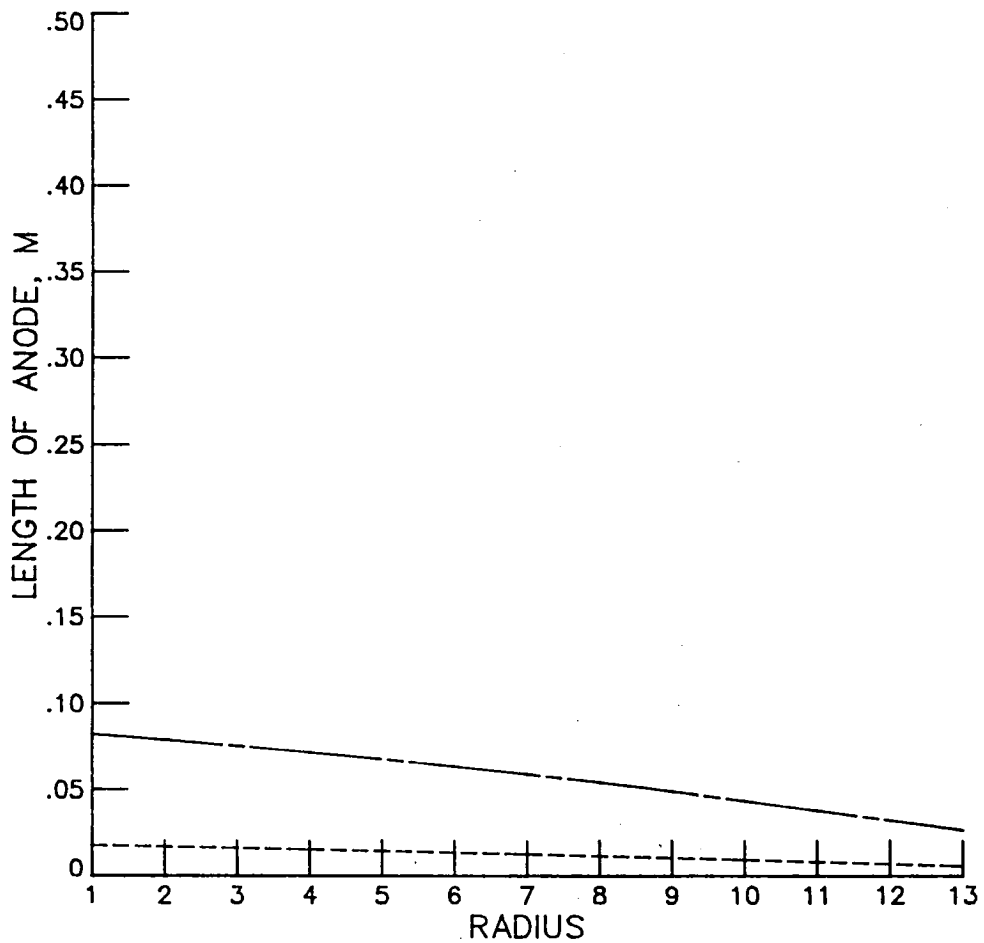


Figure 10. Current sheet locations at 3 selected times while the gas pressure was maintained at 9 mTorr and the system inductant at 100 nH. The numbers 1 and 13 are the inner and outer electrodes. The current sheet at 0.1  $\mu$ sec still stays on the initial position.

—————	TIME =	.1 $\mu$ sec
- - - - -	TIME =	.8 $\mu$ sec
—————	TIME =	3.1 $\mu$ sec

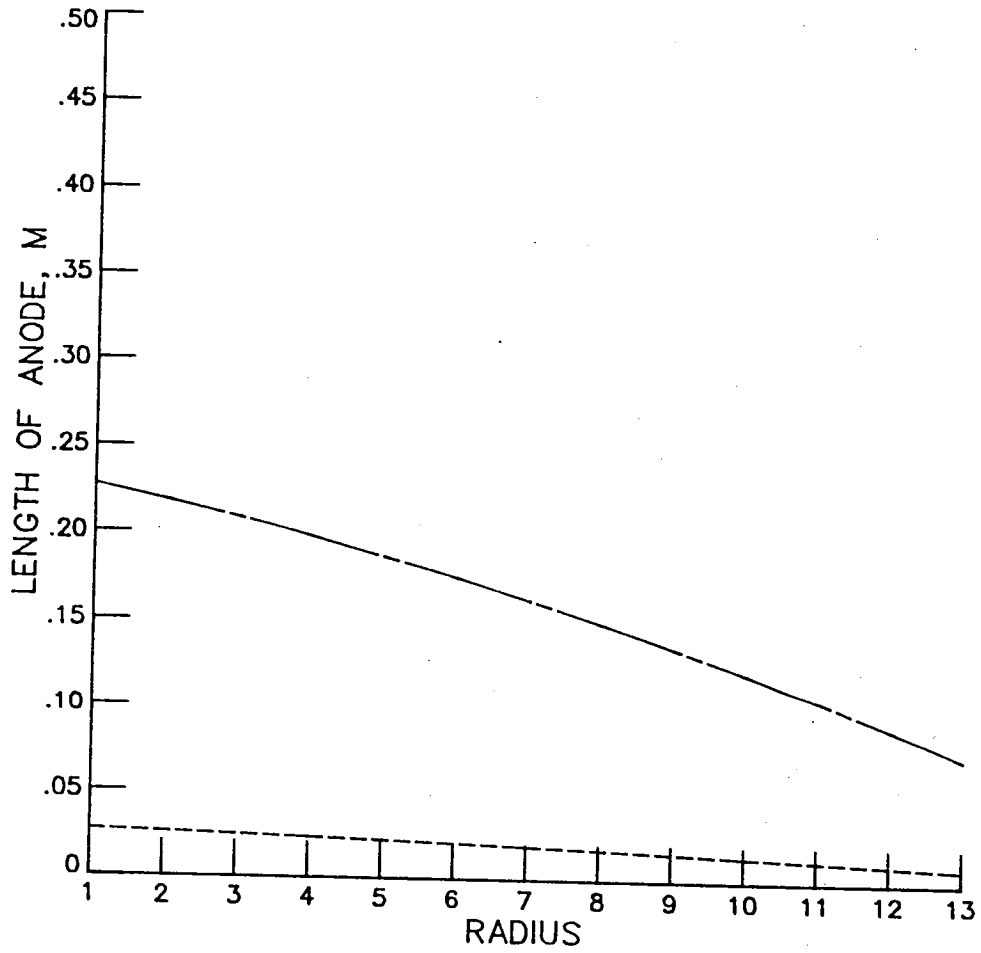


Figure 11. Current sheet location 3 selected times.  $p = 0.7$  mTorr and  $L_{\text{sys}} = 700$  nH. The current sheet at  $0.1 \mu\text{sec}$  still stays on the initial position.

————— DENR = .7073999E-03 TORR  
- - - - - DENR = .4337400E-02 TORR  
————— DENR = .7967400E-02 TORR

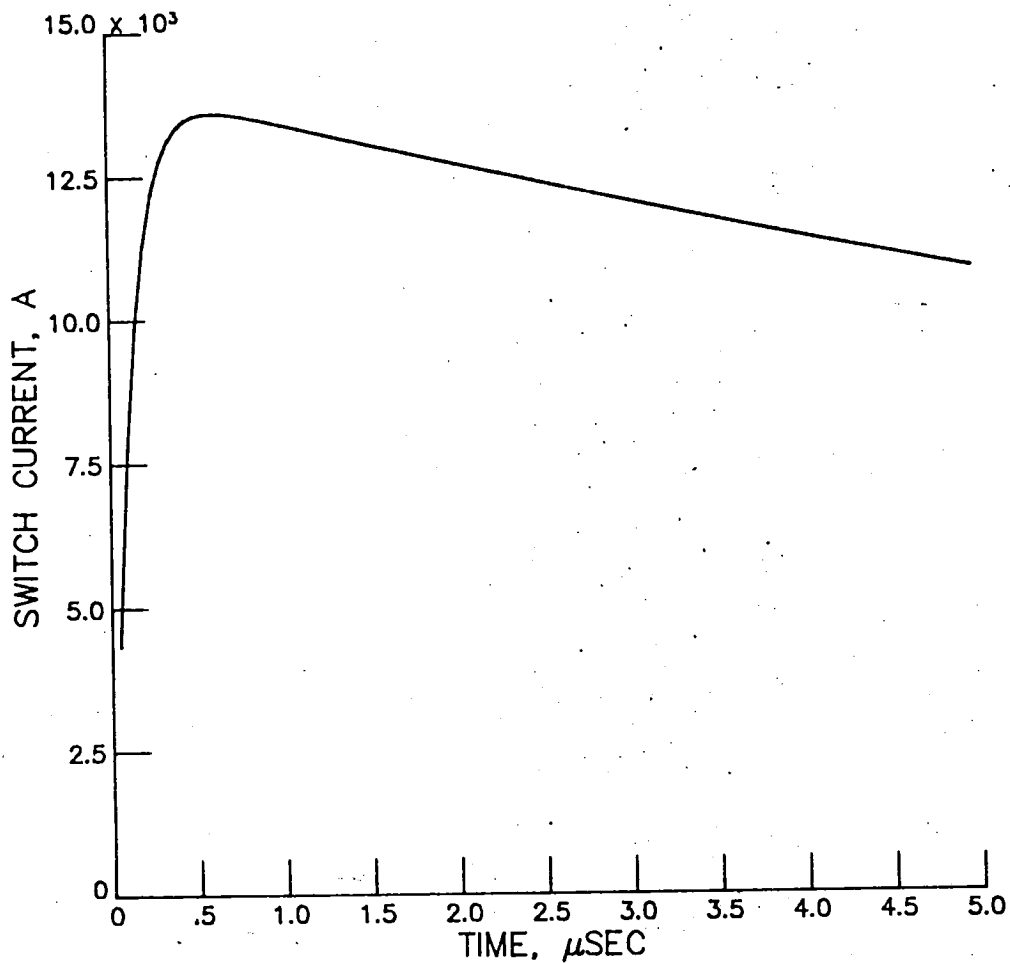


Figure 12. Discharge plasma current profile during the discharge period at 3 selected pressures, while the system inductance was maintained at 100 nH. It shows no effects on discharge plasma current due to the variation of gas pressure.

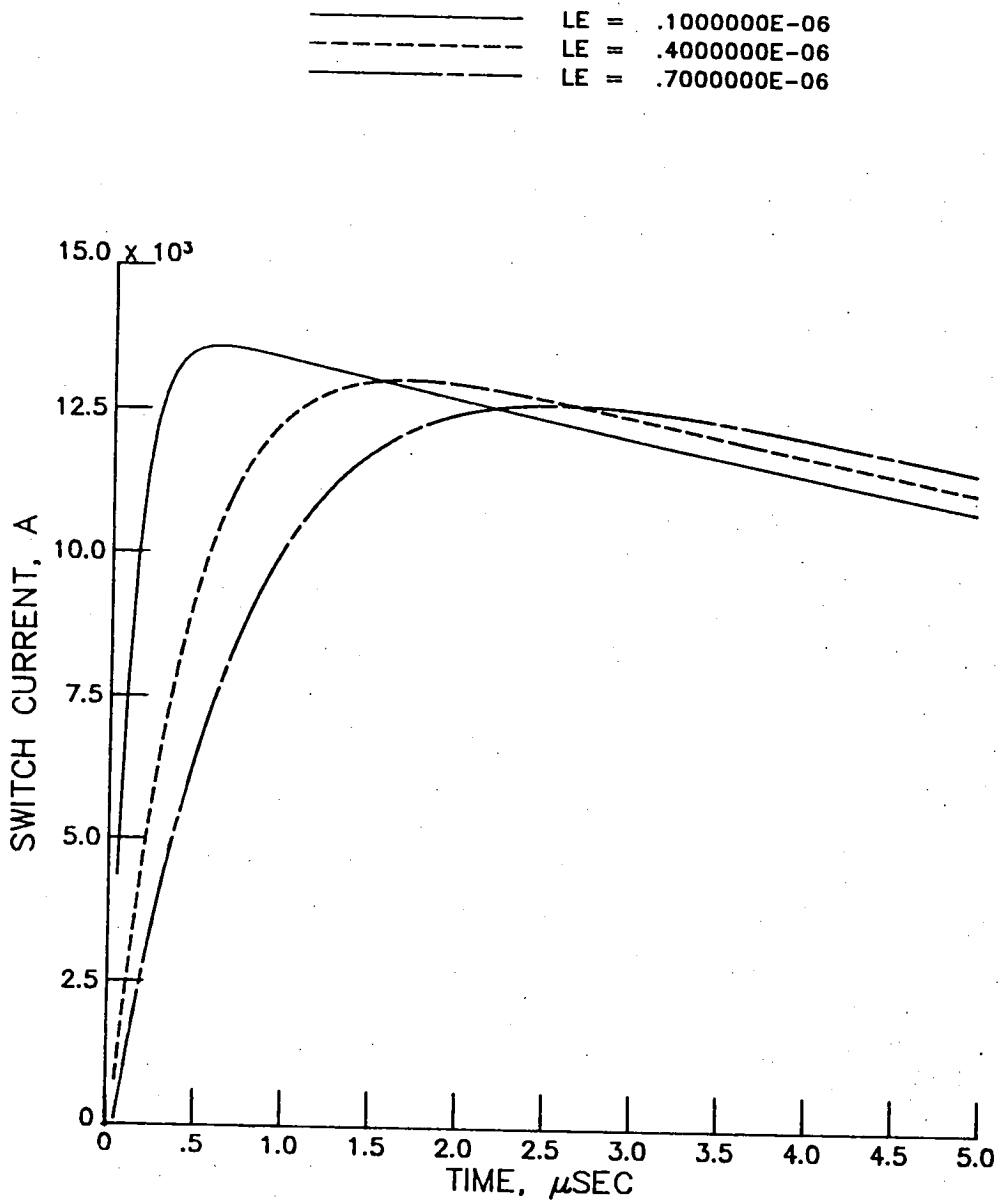


Figure 13. Discharge plasma current changes at 3 selected system inductances.  $p = 0.7$  mTorr.

\_\_\_\_\_ RADIUS = 2  
 - - - - - RADIUS = 4  
 \_\_\_\_\_ RADIUS = 6  
 - - - - - RADIUS = 8  
 \_\_\_\_\_ RADIUS = 10

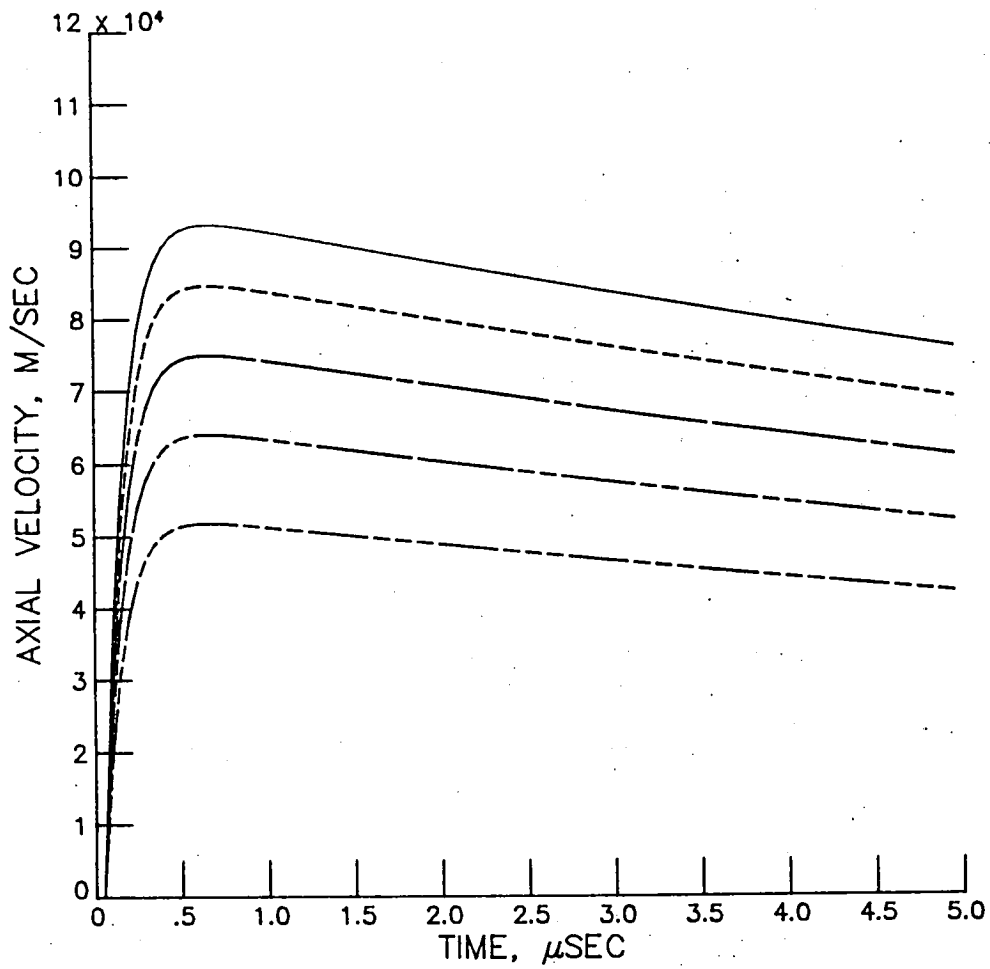


Figure 14. Axial velocities of current sheet at 5 different radial positions during the discharge period. The gas pressure was 0.7 mTorr and the system inductance was 100 nH.

—————	RADIUS = 2
- - - - -	RADIUS = 4
—————	RADIUS = 6
- - - - -	RADIUS = 8
—————	RADIUS = 10

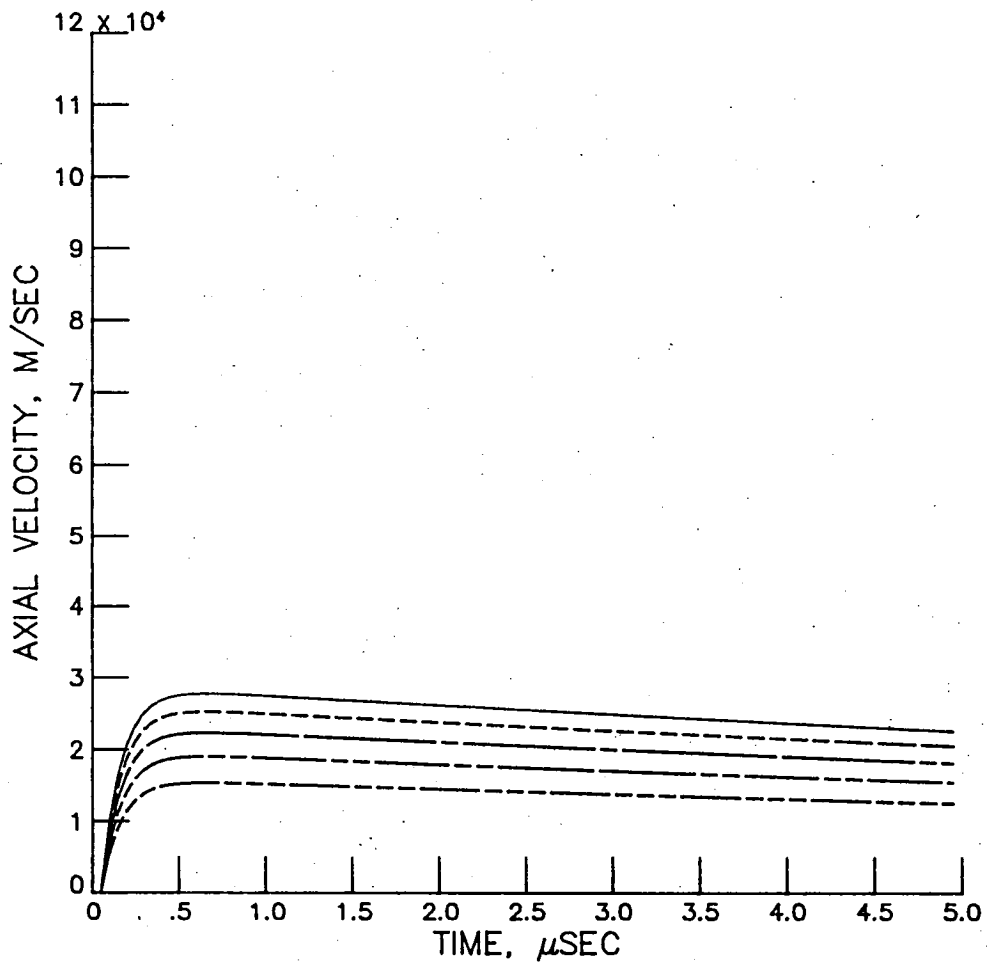


Figure 15. Axial velocities at 5 selected radial positions during the discharge period.  $p = 8$  mTorr and  $L_{sys} = 100$  nH.

—————	RADIUS = 2
- - - - -	RADIUS = 4
—————	RADIUS = 6
- - - - -	RADIUS = 8
—————	RADIUS = 10

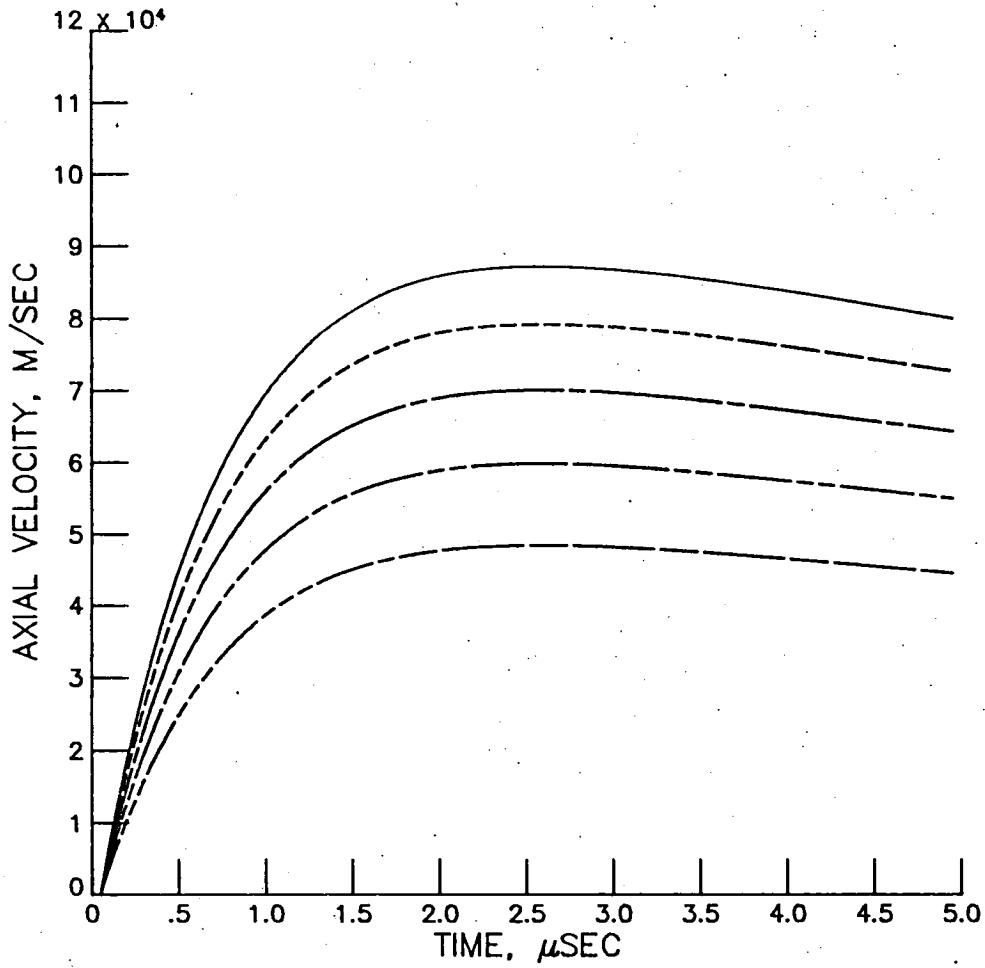


Figure 16. Axial velocities at 5 selected radial positions during the discharge period.  $p = 0.7$  mTorr and  $L_{sys} = 700$  nH.

—————	RADIUS = 2
- - - - -	RADIUS = 4
—————	RADIUS = 6
- - - - -	RADIUS = 8
—————	RADIUS = 10

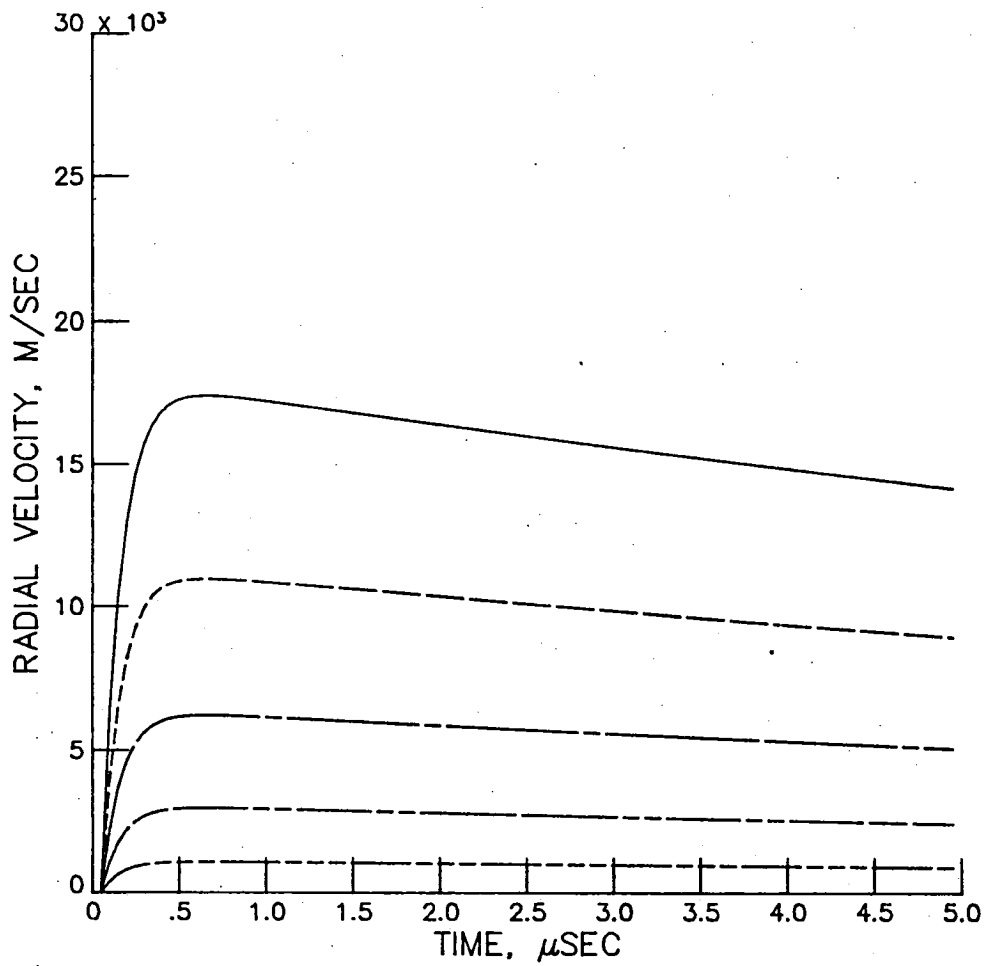


Figure 17. Radial velocities of current sheet at 5 different radial positions. The gas pressure was 0.7 mTorr and the system inductance was 100 nH.

—————	RADIUS = 2
- - - - -	RADIUS = 4
—————	RADIUS = 6
- - - - -	RADIUS = 8
—————	RADIUS = 10

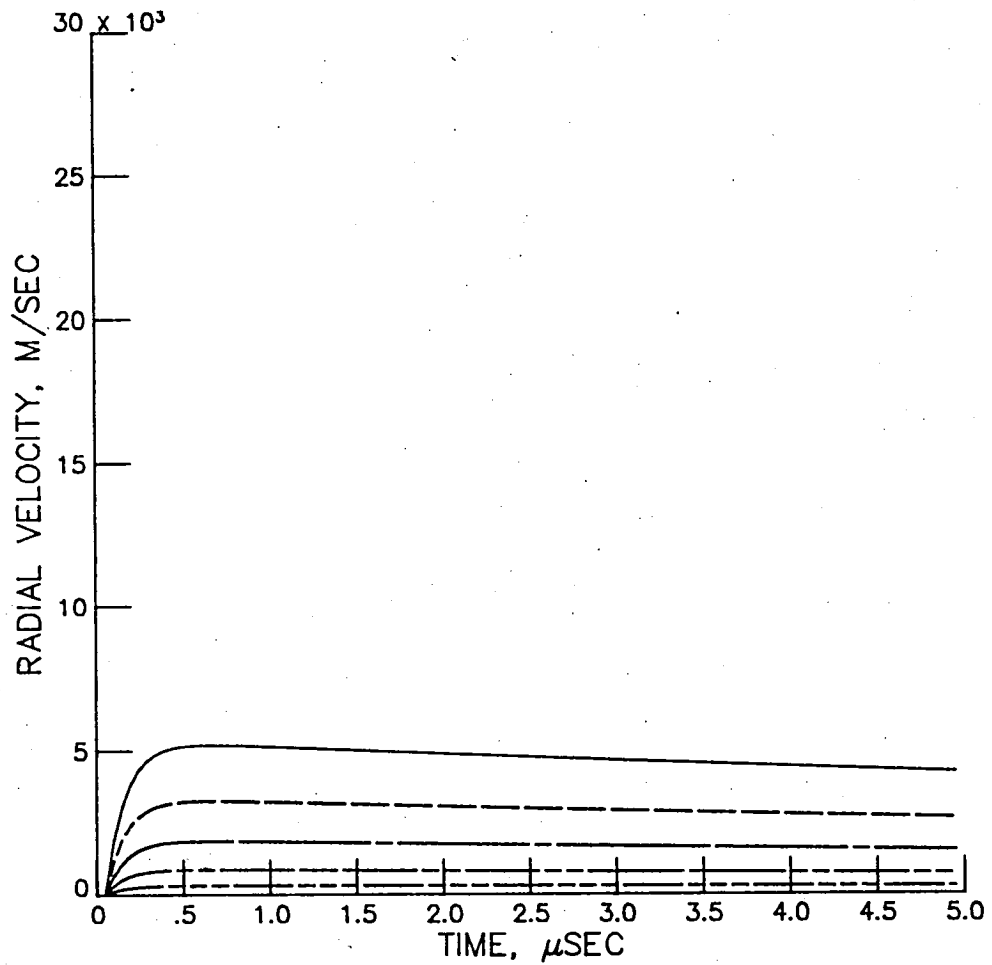


Figure 18. Radial velocities at 5 selected radial positions during the discharge period.  $p = 8$  mTorr and  $L_{\text{sys}} = 100$  nH.

—————	RADIUS = 2
- - - - -	RADIUS = 4
—————	RADIUS = 6
- - - - -	RADIUS = 8
—————	RADIUS = 10

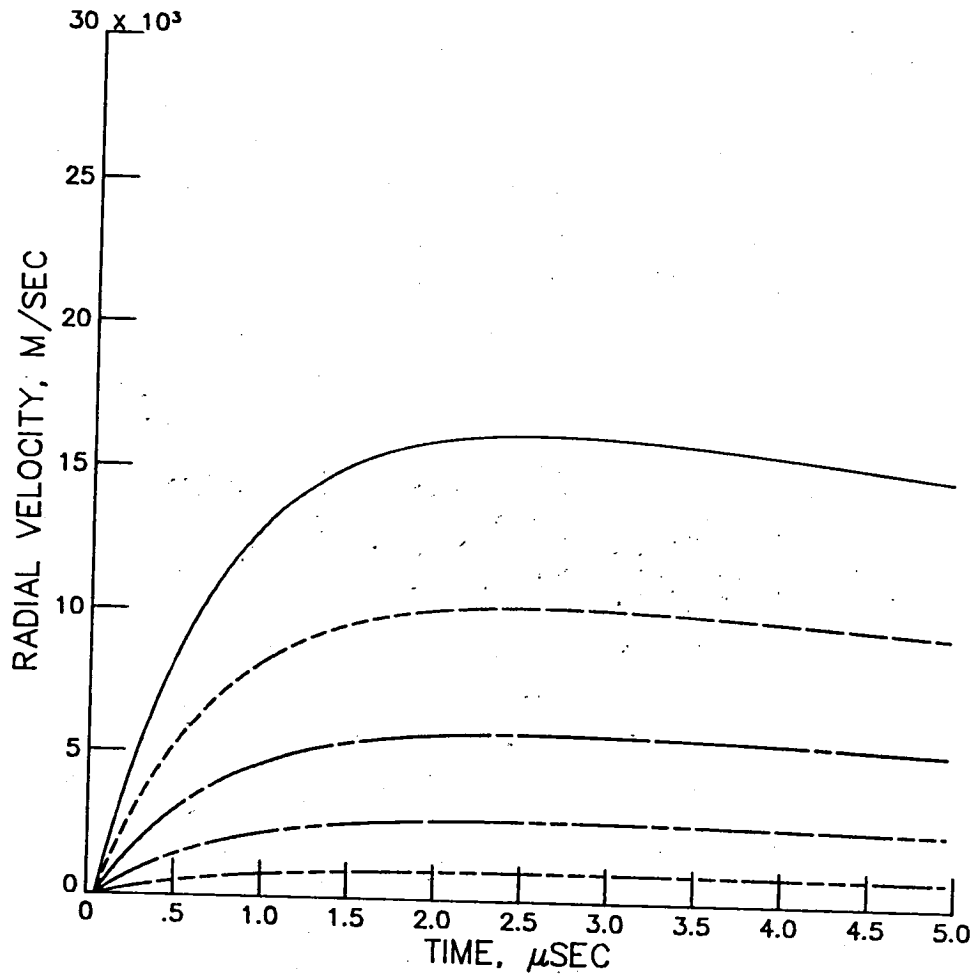


Figure 19. Radial velocities at 5 selected radial positions.  
 $p = 0.7$  mTorr and  $L_{\text{sys}} = 700$  nH.

\_\_\_\_\_ TIME = .1  $\mu$ sec  
 - - - - - TIME = .8  $\mu$ sec  
 \_\_\_\_\_ TIME = 3.1  $\mu$ sec

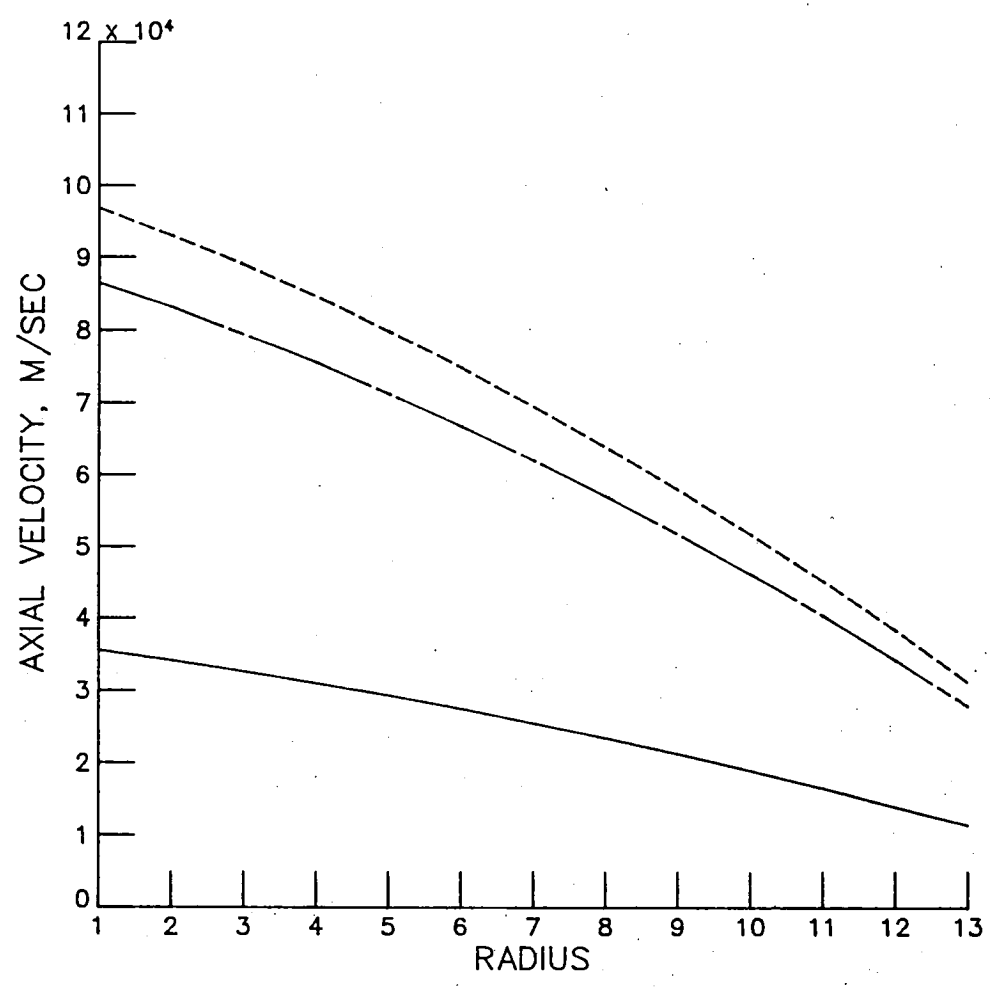


Figure 20. Axial velocities along the radial direction at 3 selected discharge times. The gas pressure was 0.7 mTorr and the system inductance was 100 nH. The numbers 1 and 13 on the Radius axis are the inner ( $r_i = 0.0365$  m) and the outer ( $r_o = 0.0643$  m) electrodes radius.

\_\_\_\_\_ TIME = .1  $\mu$ sec  
 - - - - - TIME = .8  $\mu$ sec  
 \_\_\_\_\_ TIME = 3.1  $\mu$ sec

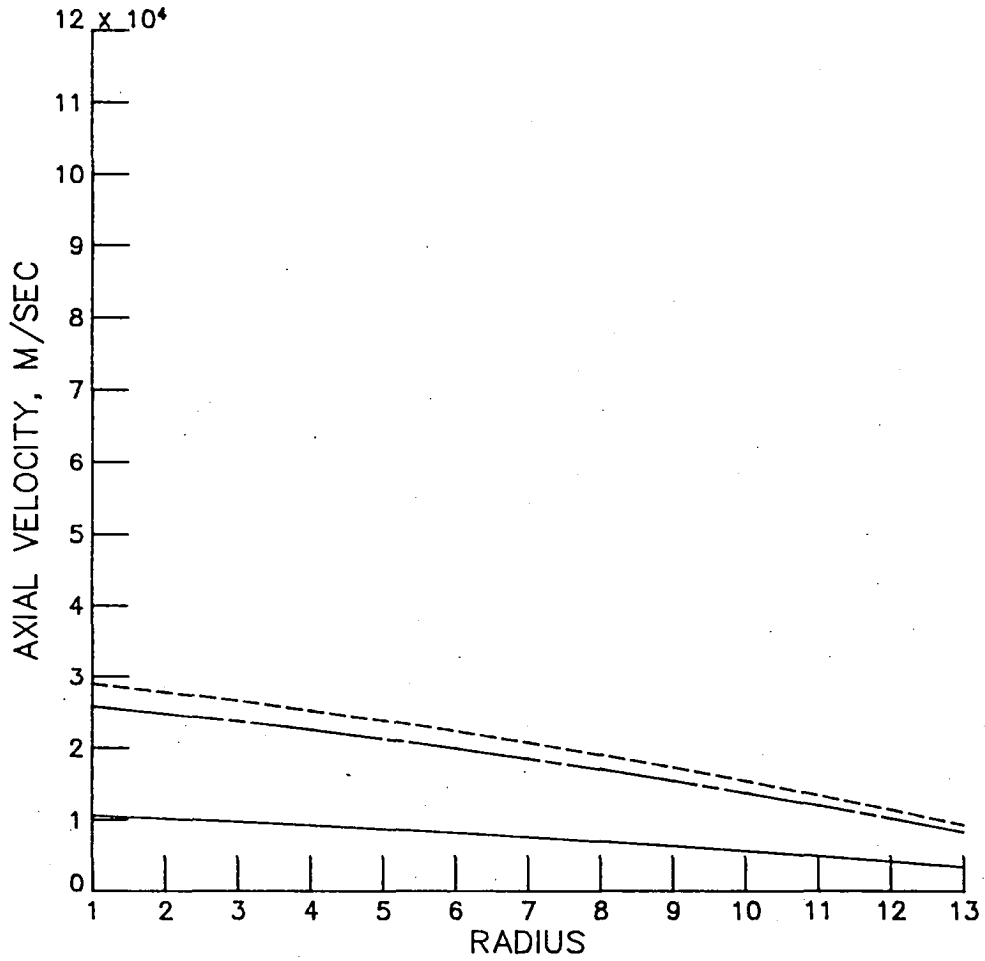


Figure 21. Axial velocities at 3 selected times along the radial direction.  $p = 8$  mTorr and  $L_{sys} = 100$  nH.

—————	TIME =	.1 $\mu$ sec
- - - - -	TIME =	.8 $\mu$ sec
—————	TIME =	3.1 $\mu$ sec

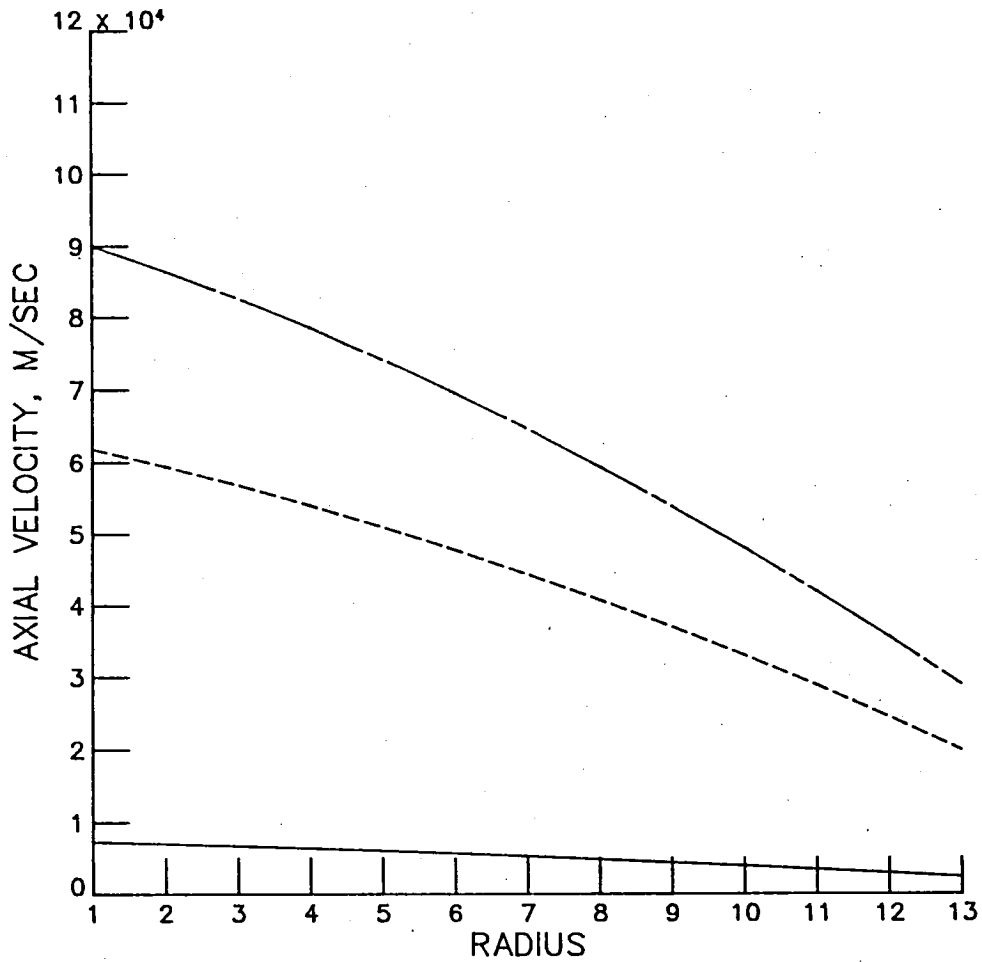


Figure 22. Axial velocity profiles at 3 selected times.  
 $p = 0.7$  mTorr and  $L_{\text{sys}} = 700$  nH.

TIME = .8  $\mu$ sec

————— DENR = .7073999E-03 TORR  
- - - - - DENR = .4337400E-02 TORR  
————— DENR = .7967400E-02 TORR

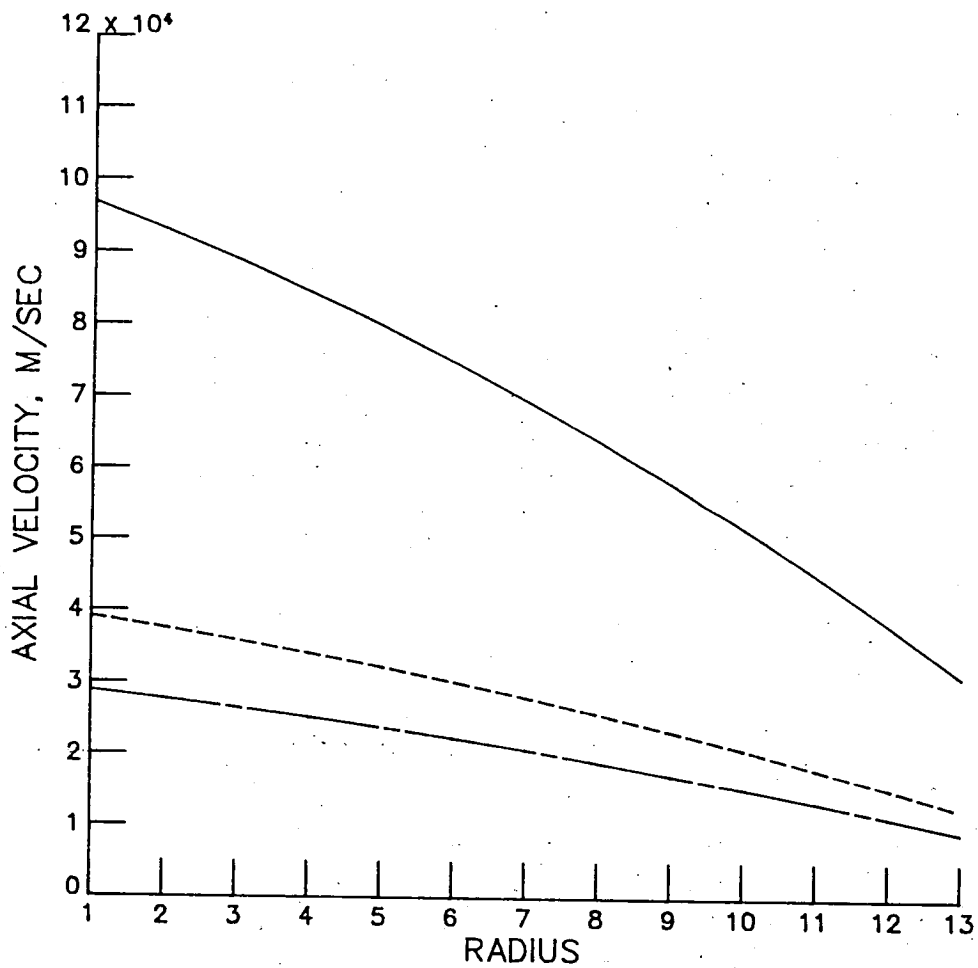


Figure 23. Axial velocities at 3 selected pressures and at 0.8  $\mu$ sec after the discharge began.  $L_{sys} = 100$  nH.

TIME = .8  $\mu$ sec

————— LE = .1000000E-06  
- - - - - LE = .4000000E-06  
————— LE = .7000000E-06

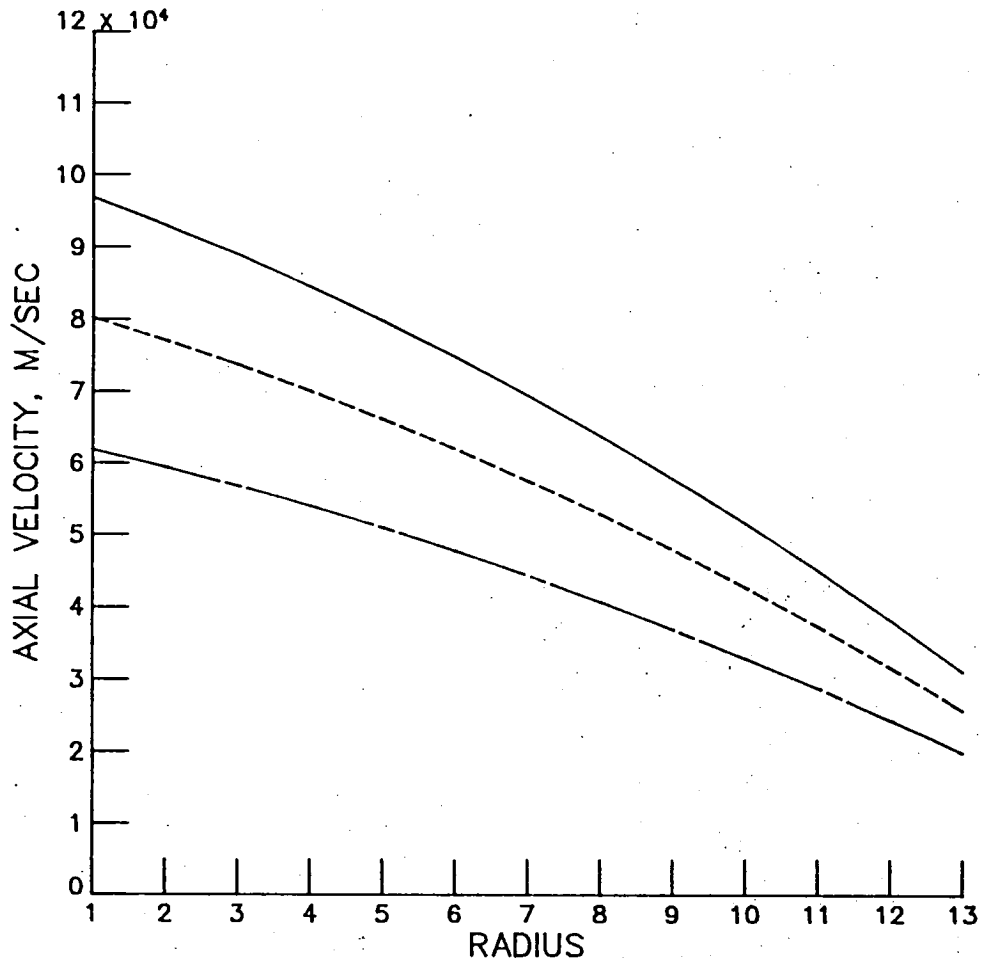


Figure 24. Axial velocity profiles between electrodes (1 and 13) at 3 selected system inductances and at 0.8 $\mu$  sec after the discharge began.  $p = 0.7$  mTorr.

—————	TIME =	.1 $\mu\text{sec}$
- - - - -	TIME =	.8 $\mu\text{sec}$
—————	TIME =	3.1 $\mu\text{sec}$

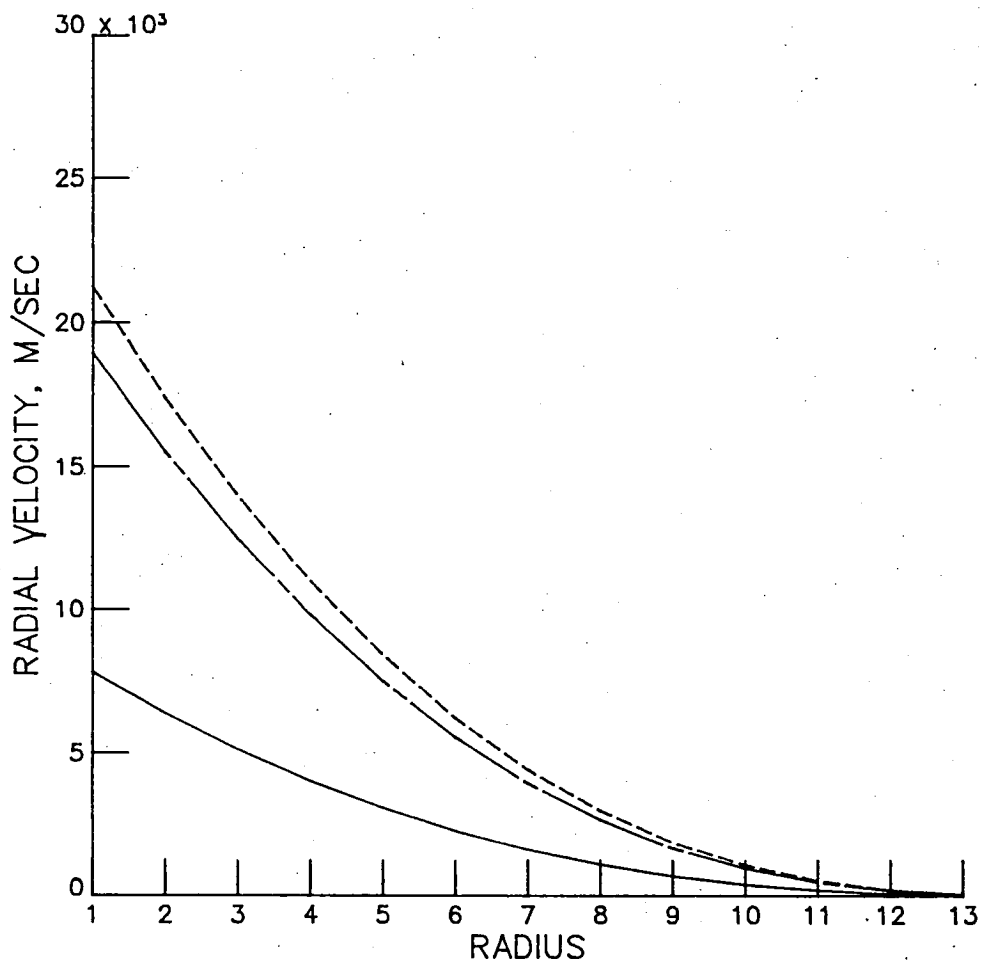


Figure 25. Radial velocities along the radial direction at 3 selected discharge times. The gas pressure was 0.7 mTorr and the system inductance 100 nH. The numbers 1 and 13 on Radius axis are the inner ( $r_1 = 0.0365$  m) and the outer ( $r_0 = 0.0643$  m) electrodes radius.

—————	TIME =	.1 $\mu$ sec
- - - - -	TIME =	.8 $\mu$ sec
—————	TIME =	3.1 $\mu$ sec

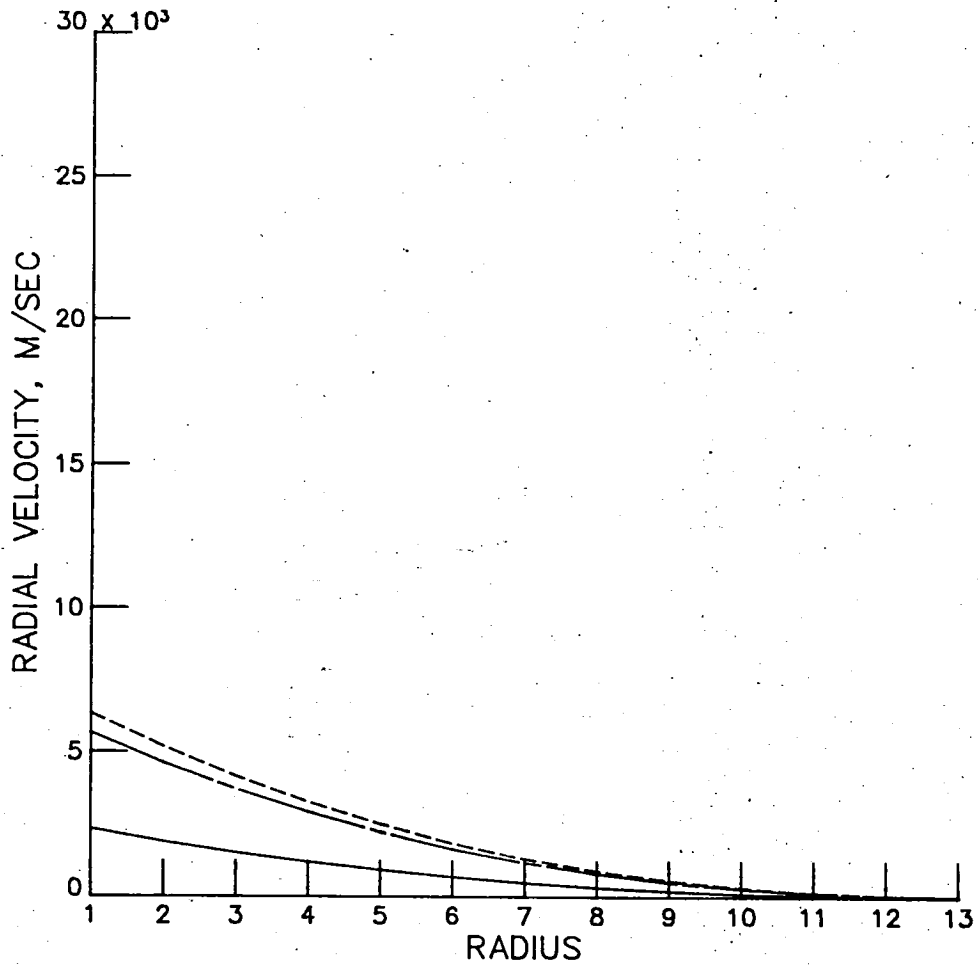


Figure 26. Radial velocities at 3 selected times along the radial direction.  $p = 8$  mTorr and  $L_{\text{sys}} = 100$  nH.

————— DENR = .7073999E-03 TORR  
- - - - - DENR = .4337400E-02 TORR  
————— DENR = .7967400E-02 TORR

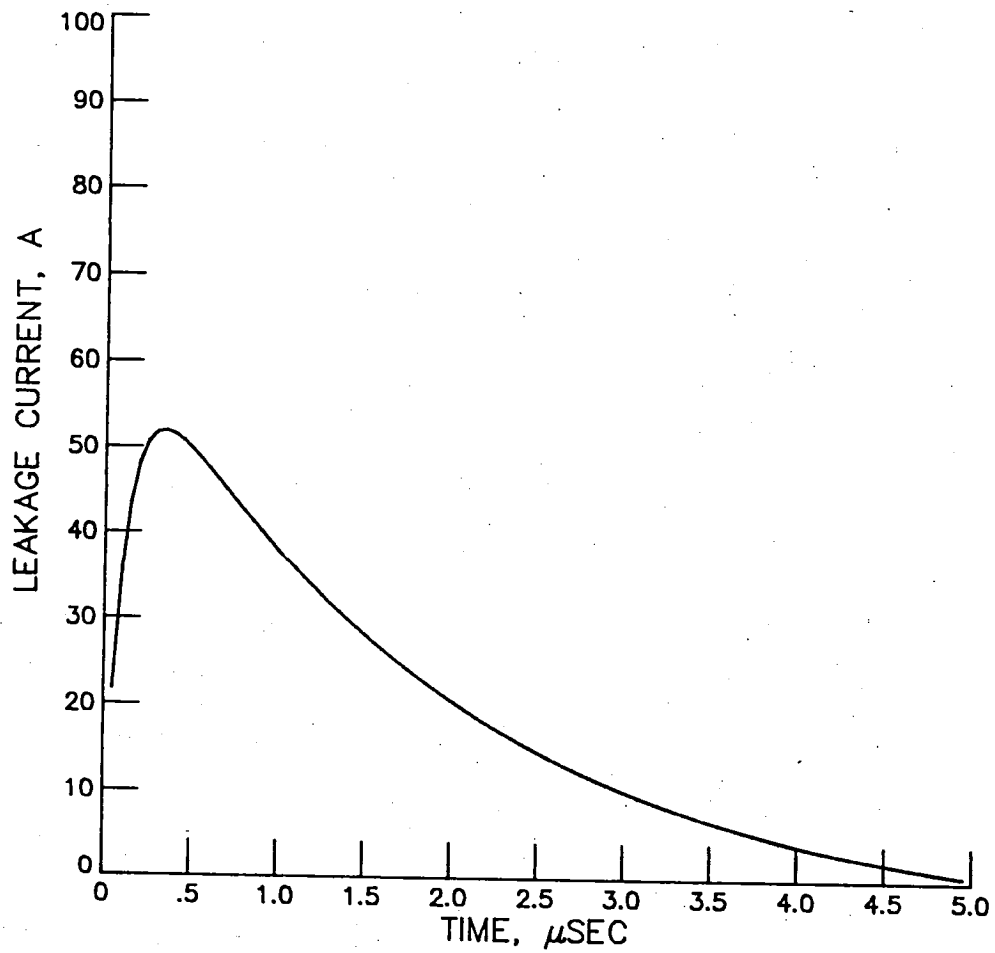


Figure 27. Leakage current during the discharge period at 3 selected pressures, while  $L_{sys} = 100$  nH. It shows no effects on leakage current due to the variation of gas pressure.

—————	LE = .1000000E-06
- - - - -	LE = .4000000E-06
—————	LE = .7000000E-06

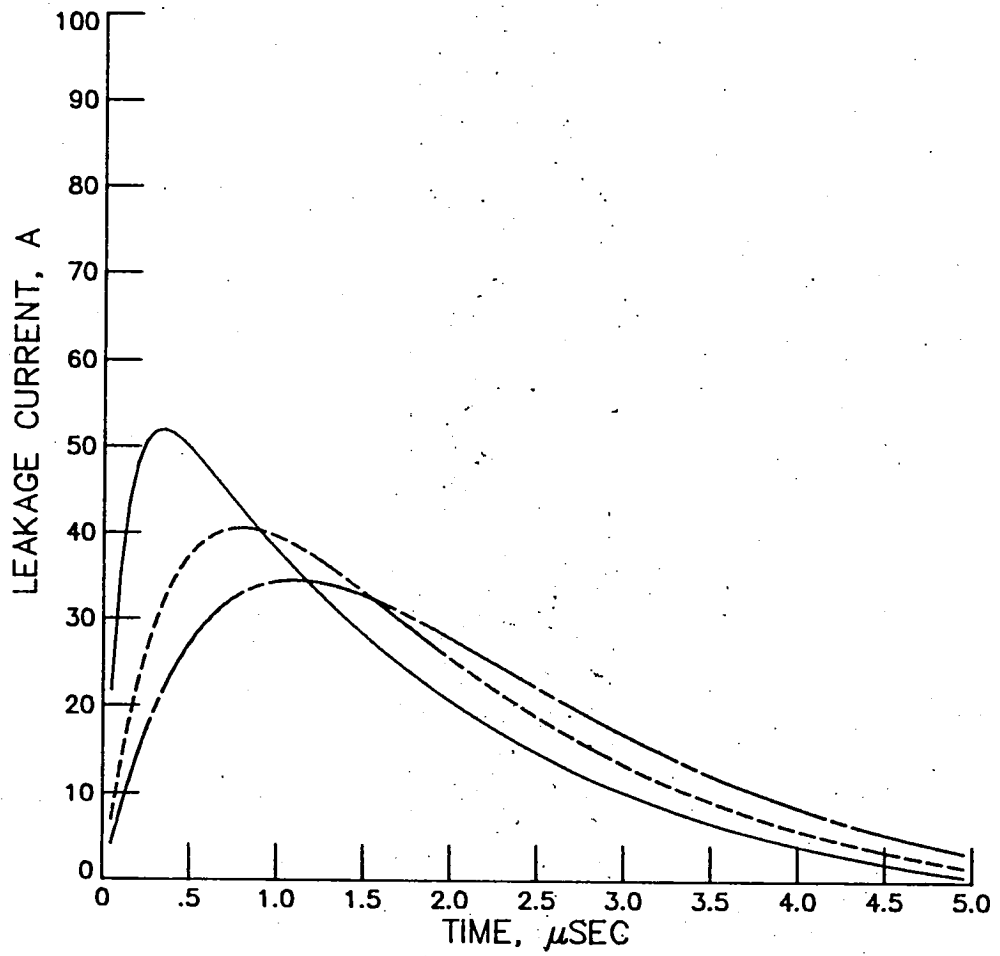


Figure 28. Leakage currents at selected system inductances  
 $p = 0.7$  mTorr.

————— LE = .1000000E-06  
- - - - - LE = .4000000E-06  
————— LE = .7000000E-06

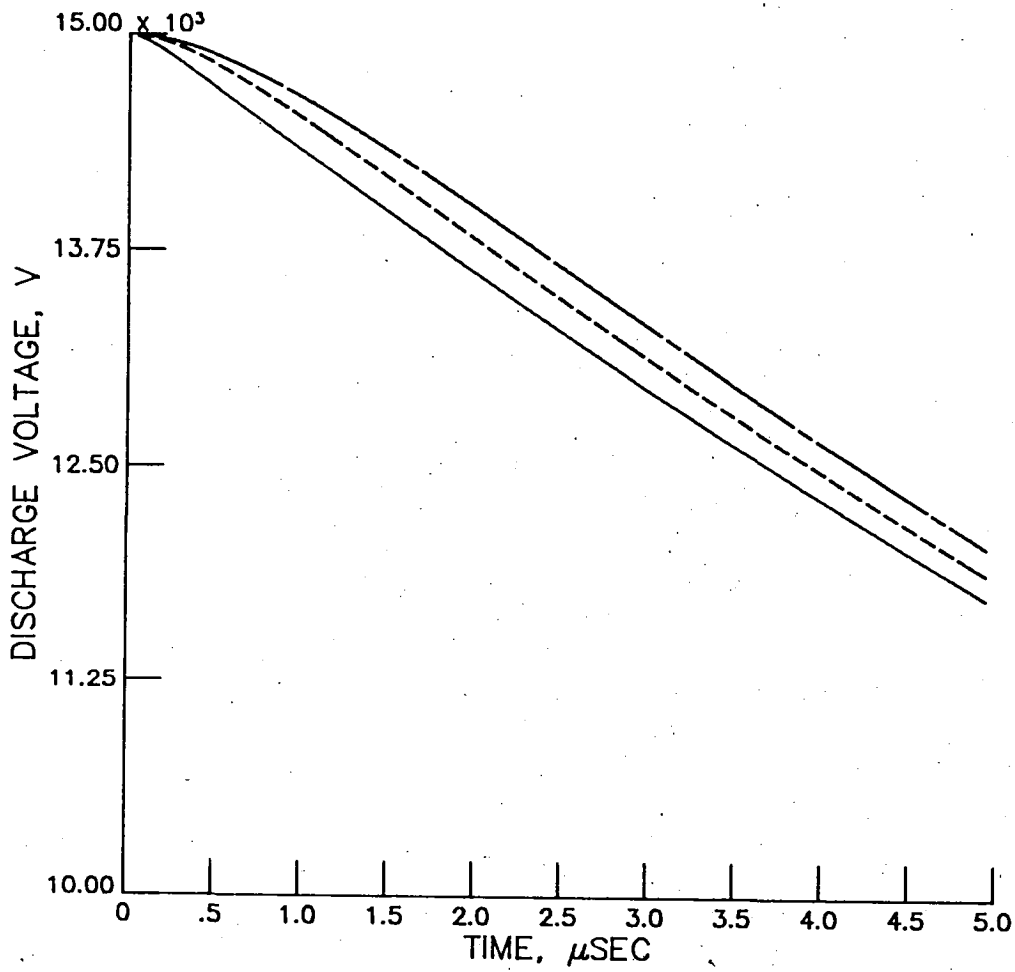


Figure 29. Discharge voltage variations at 3 selected system inductances during the discharge period.

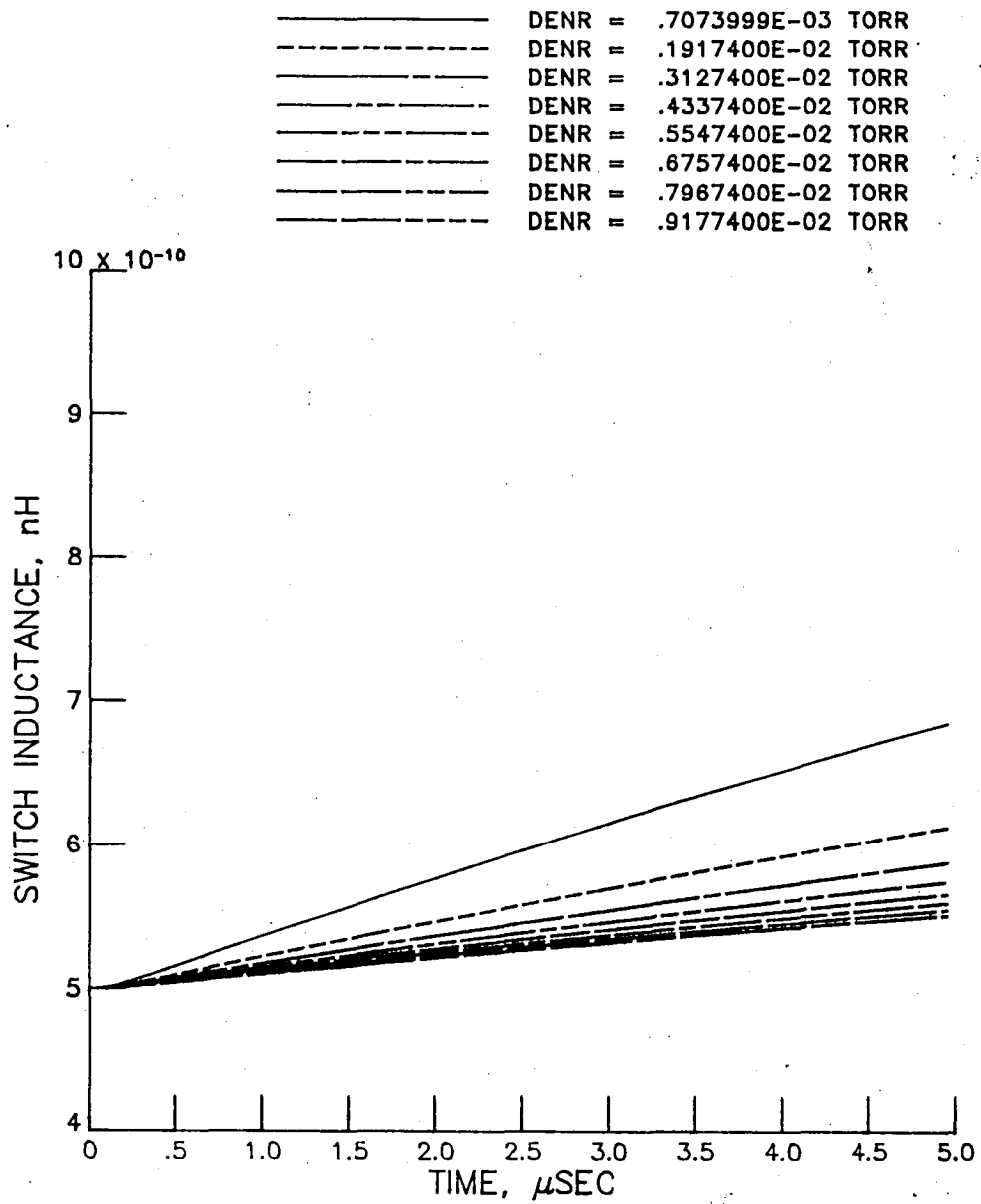


Figure 30. Switch inductances at 8 selected pressures during the discharge period.  $L_{sys} = 100$  nH.

## REFERENCES

1. M. Kristiansen, et al., "Opening Switches", IEEE Conference Record 81CH1640-5 NPS , 67, 1981.
2. M. Gundersen, "Optical Processes in Lower-Controller Gas-Phase Switches", Electro-Optical Systems, Design, pp. 25-33, June 1982.
3. Proceedings of International Conference on Energy Storage, Compression, and Switching, Nov. 5-7, 1974, Torino, Italy.
4. C. W. Kimblin, "Anode Phenomena in Vacuum and Atmospheric Pressure Arcs", IEEE Trans. Plasma Sci. PS-2, 310 (1974).
5. D. R. Porto and C. W. Kimblin, "Cathode Spot Phenomena in the Transition from Vacuum to Atmospheric Pressure Arcs", IEEE Conference, Record 81Ch1640-2 NPS, 87 (1981).
6. H. H. Lee, "High Coulomb Transfer Switch (HCTS)", U. S. Patent No. 4,475,066 issued October 2, 1984.
7. S. H. Choi and J. H. Lee, "An Inverse-Pinch Switch for High Coulomb Transfer", Proceedings of the 10th IEEE International Symposium on Discharges and Electrical Insulation in Vacuum, October 25-28, 1982, Columbia, SC, p. 273.
8. S. Maxon and J. Eddleman, "Two-Dimensional Magnetohydrodynamic Calculations for the Plasma Focus", Phys. Fluids, 21, 1856 (1978).
9. Eltgroth, P. G.: "Comparison of Plasma Focus Calculations". The Physics of Fluids, 25 (12), December 1982.

## APPENDIX A

A new type of an inverse switch was designed and built during the period of the contract. The switch was installed onto a high power source in the laboratory of Space Technology Branch. Its trigger mechanism (HCP plasma puff) and high power load are currently being tested to determine the uniformity of trigger puff and voltage hold-off.

The drawings of the switch parts are attached with an assembly drawing. As a result of testing, minor changes or corrections of the switch configuration were made for possible improvement of switch performance. Therefore, assembly and parts drawings attached here might show some differences because the recent changes were not included in the drawings.

Figure A-1 shows the assembly drawings of a new switch. The numbers on the drawings designates the parts. The list of drawings follows:

- Fig. A     Assembly Drawing
- Fig. A-1   Observation View Window
- Fig. A-2   Anode Electrode Head-disk
- Fig. A-3   Switch Chamber Housing (top)
- Fig. A-4   HCP Plasma Trigger Insulator
- Fig. A-5   Switch Chamber Housing (bottom)
- Fig. A-6   Cathode Electrode
- Fig. A-7   Switch Support Substrate
- Fig. A-8   Switch Insulator Between Anode and Cathode
- Fig. A-9   Anode Electrode Column
- Fig. A-10  Anode Electrode Cable Connector
- Fig. A-11  Electric Coaxial Cable Connector Frame

Fig. A-12 Assembly of HCP Plasma Puff Trigger

Fig. A-13 Connectors between View Window (A-1) and substrate  
(A-7). (not shown in Fig. A).

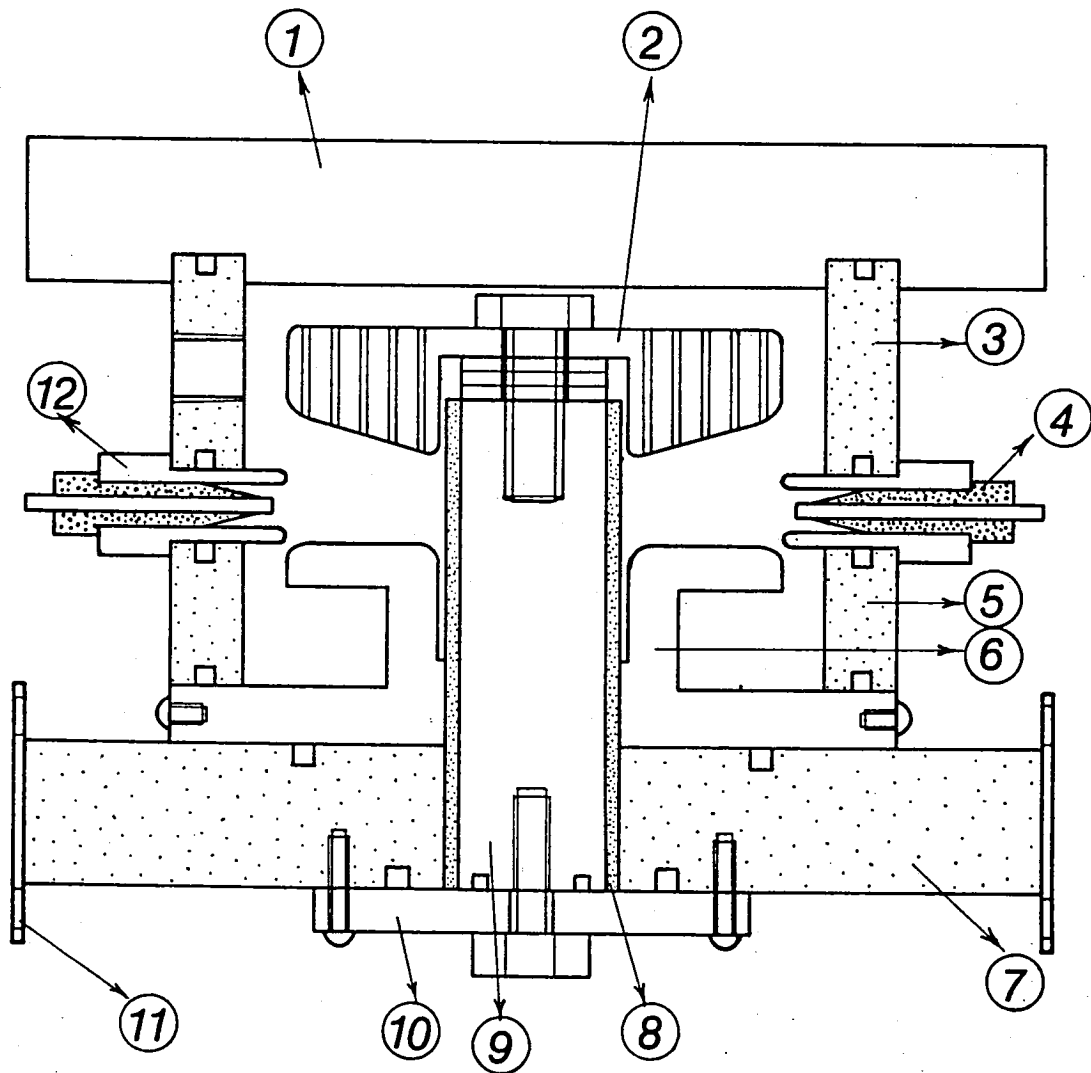


Figure A. Assembly drawing of a New Inverse-Pinch Switch. The numbers in the circles show part serial number which is the same as the figure number  
 Scale: 1/1.

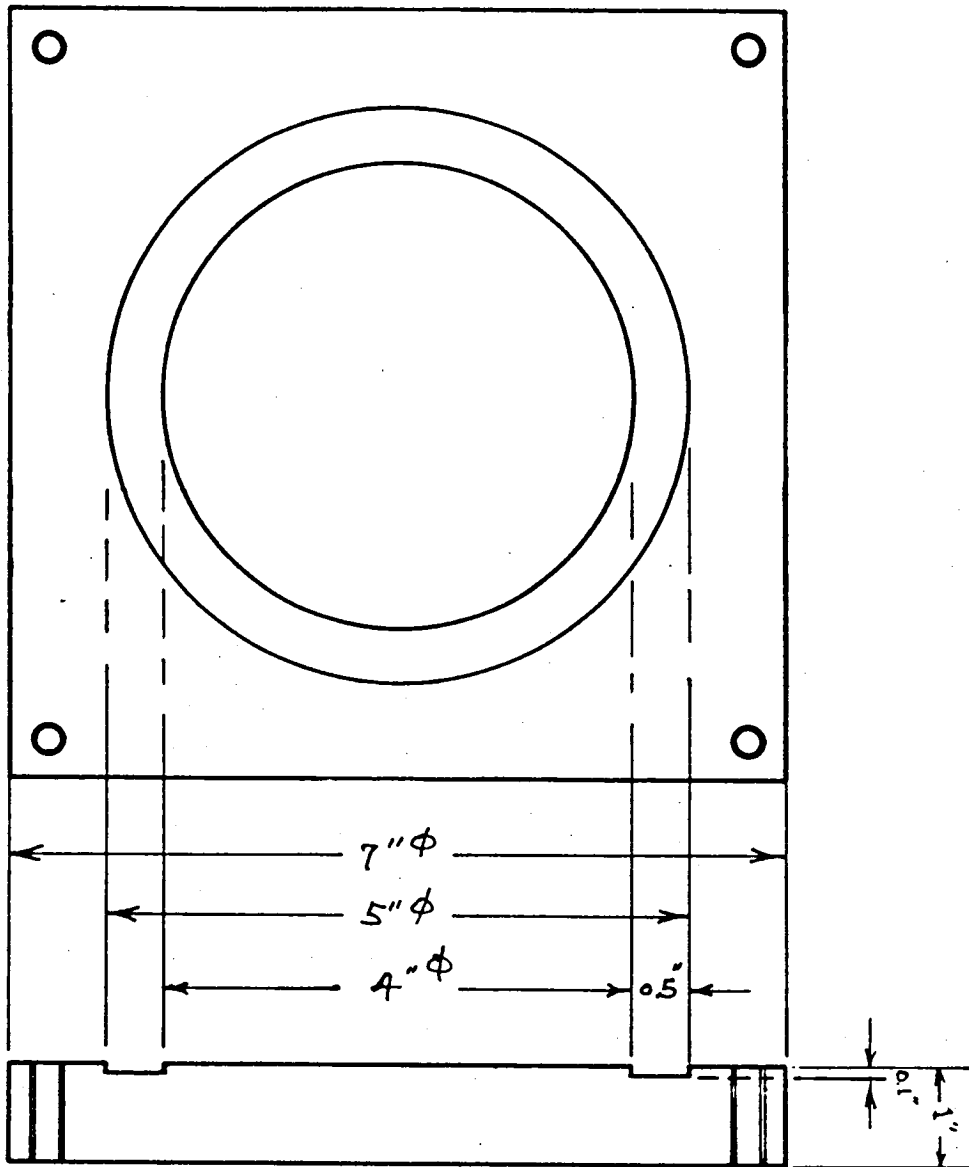


Figure A-1. Observation View Window  
Material: Plexiglas  
Scale: 1/2

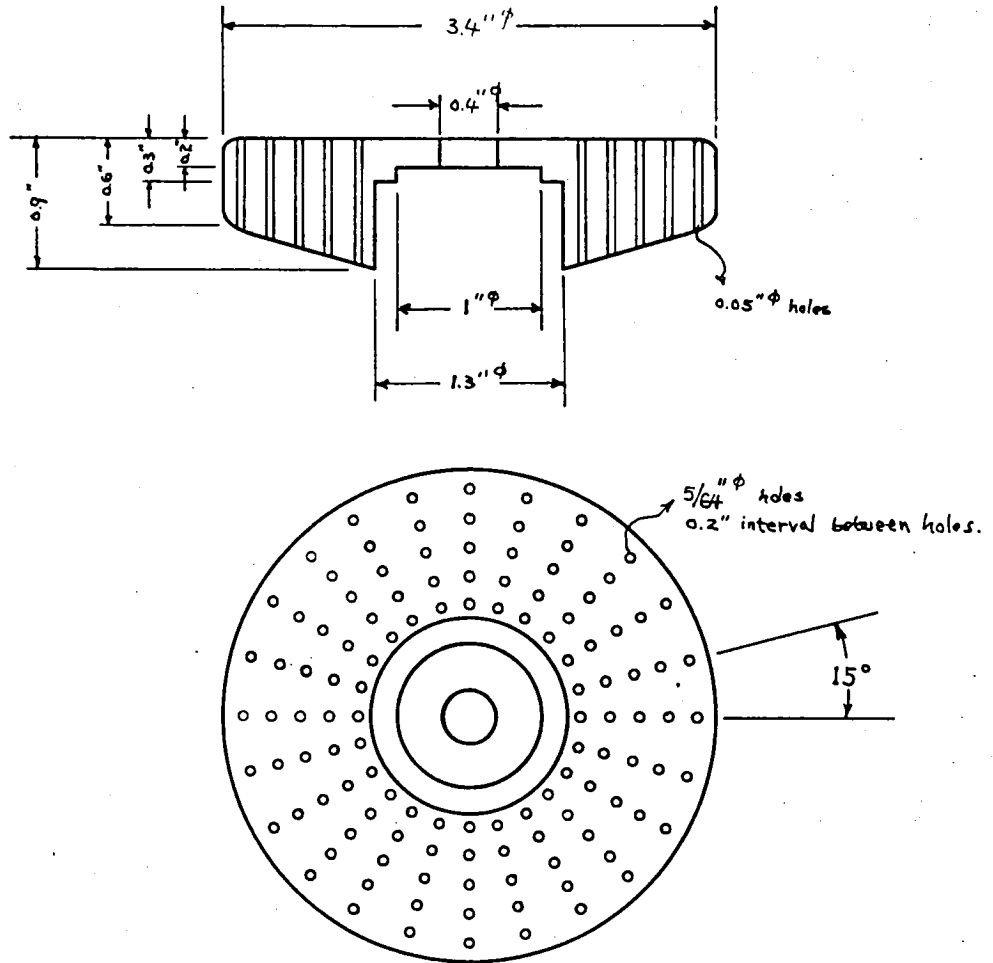


Figure. A-2. Anode Electrode head disk  
 Material: Brass  
 Scale: 1/2

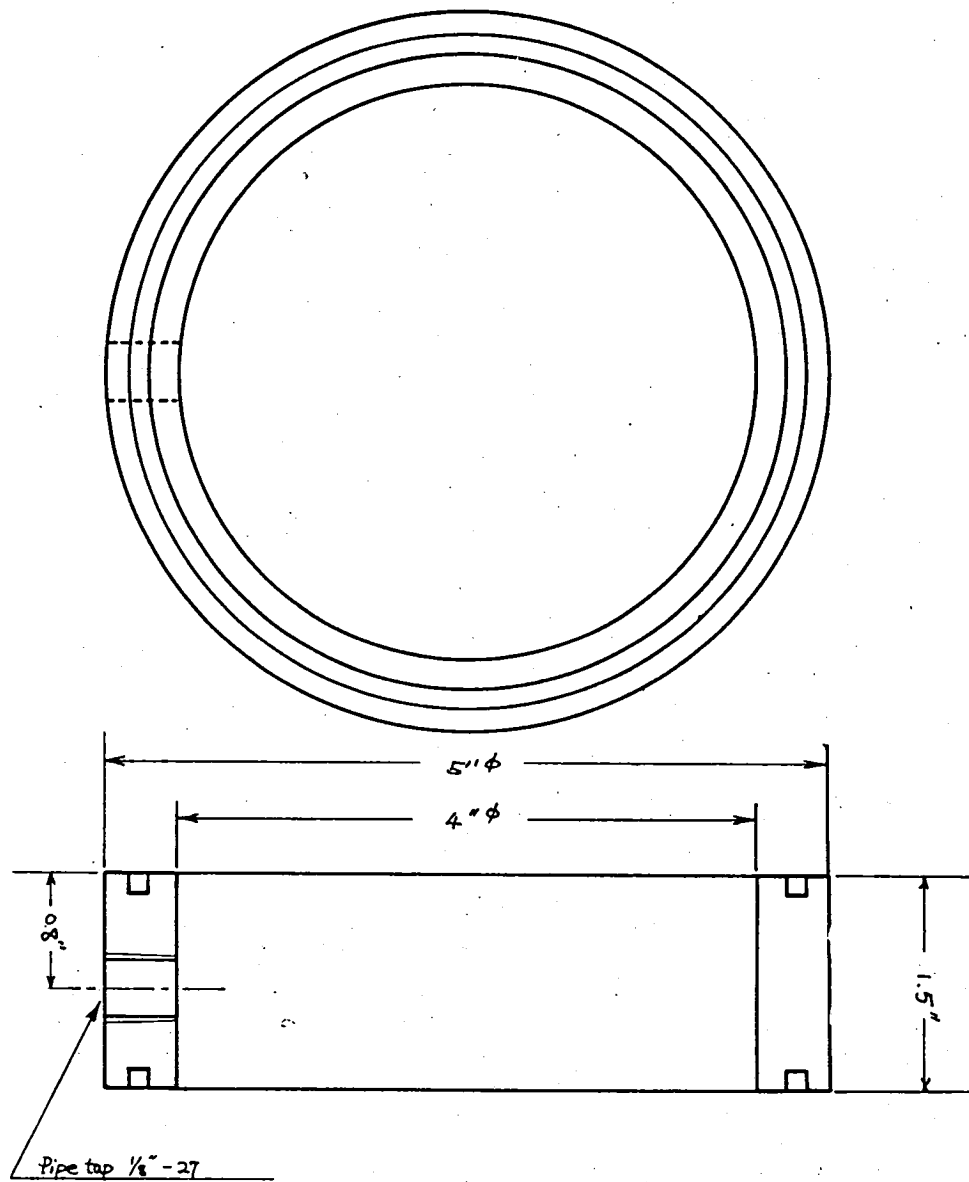


Figure. A-3. Switch Chamber Housing: Top part.  
 Material: Plexiglas  
 Scale: 1/2

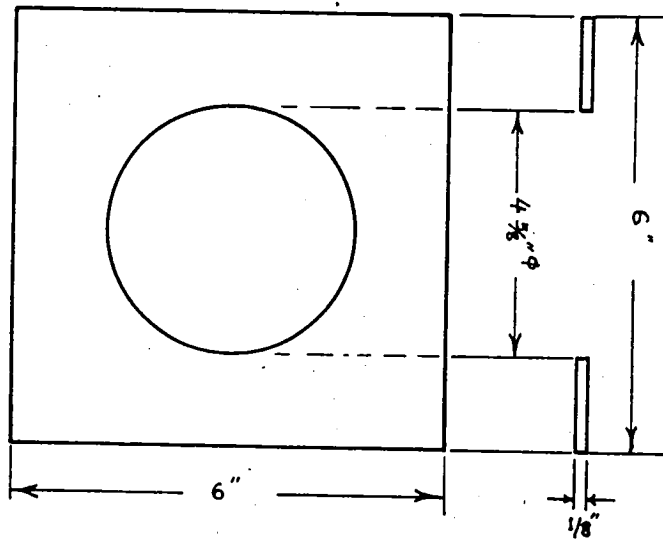


Figure. A-4. HCP Plasma Trigger Insulator  
Material: Macor  
Scale: 1/2  
No. of Pieces: 2 ea.

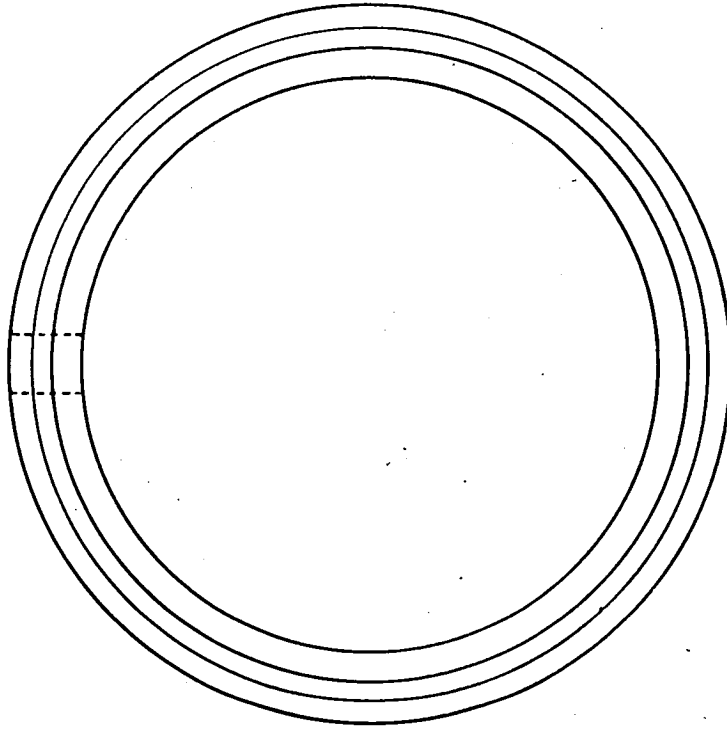
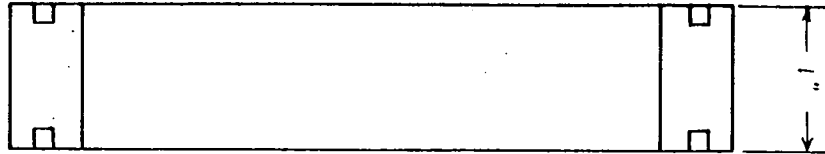


Figure. A-5. Switch Chamber Housing: Bottom part  
Material: Plexiglas  
Scale: 1/2

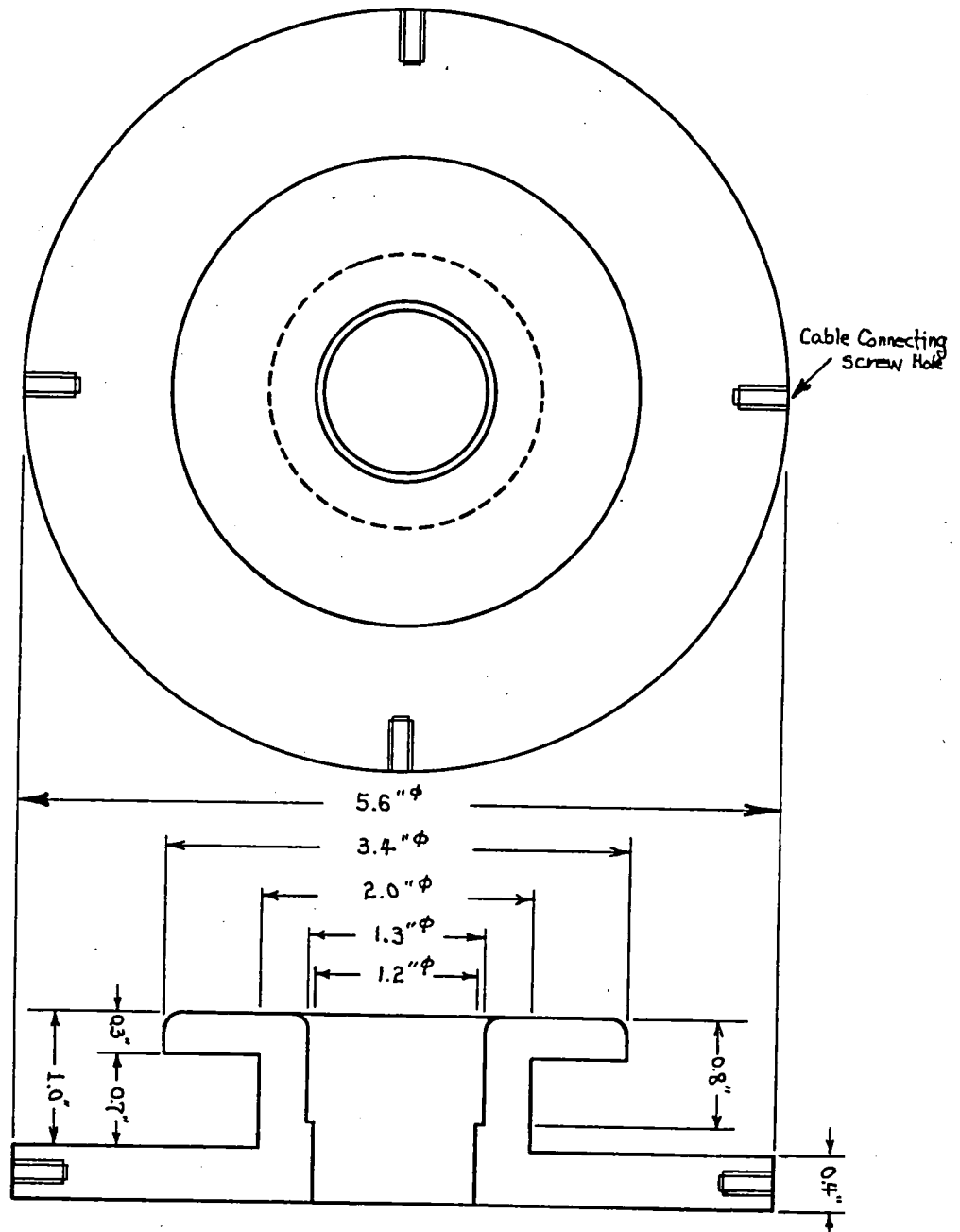


Figure. A-6. Cathode Electrode  
 Material: Brass  
 Scale: 1/2.

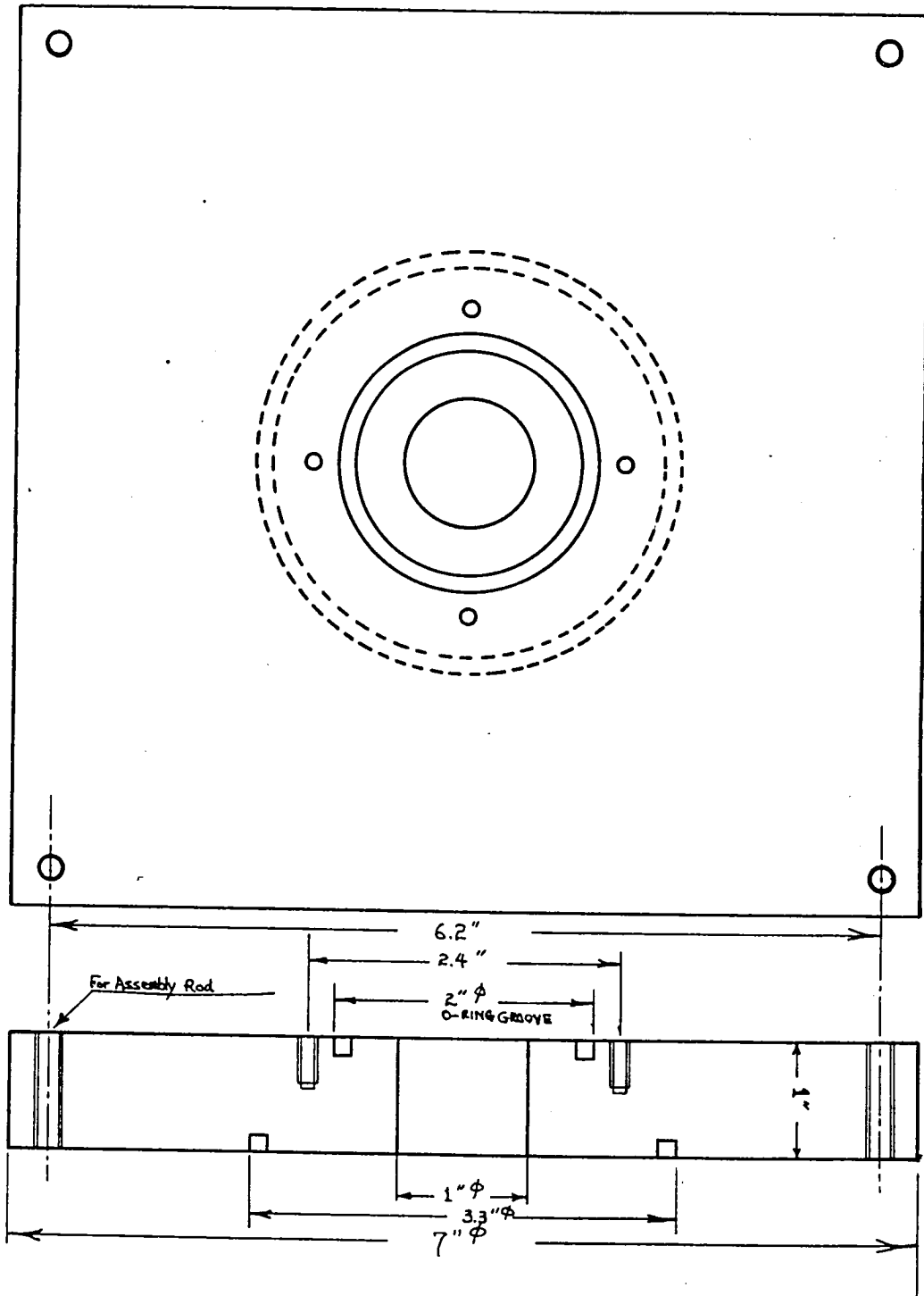


Figure. A-7. Switch Support Substrate  
 Material: Plexiglas  
 Scale: 1/2

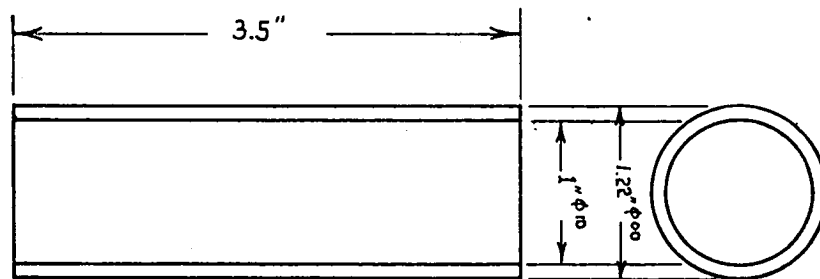


Figure. A-8. Switch Insulator  
Material: Macor  
Scale: 1/2

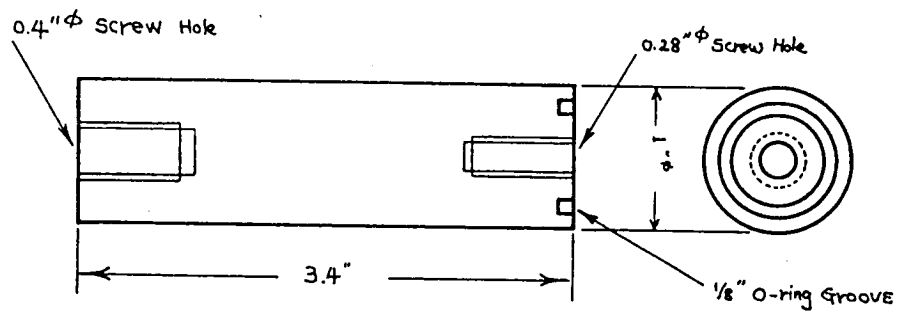


Figure. A-9. Anode Electrode Column  
Material: Brass  
Scale: 1/2

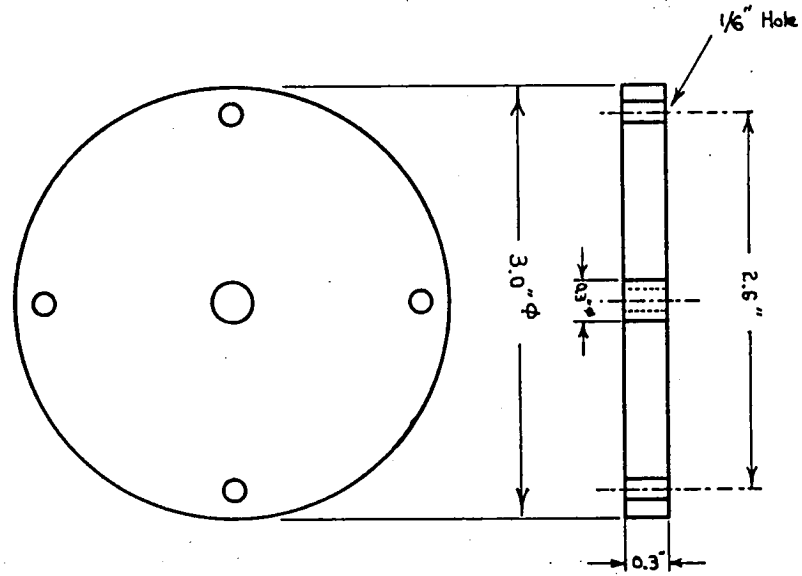


Figure. A-10. Anode Electrode Cable Connector  
Material: Brass  
Scale: 1/2

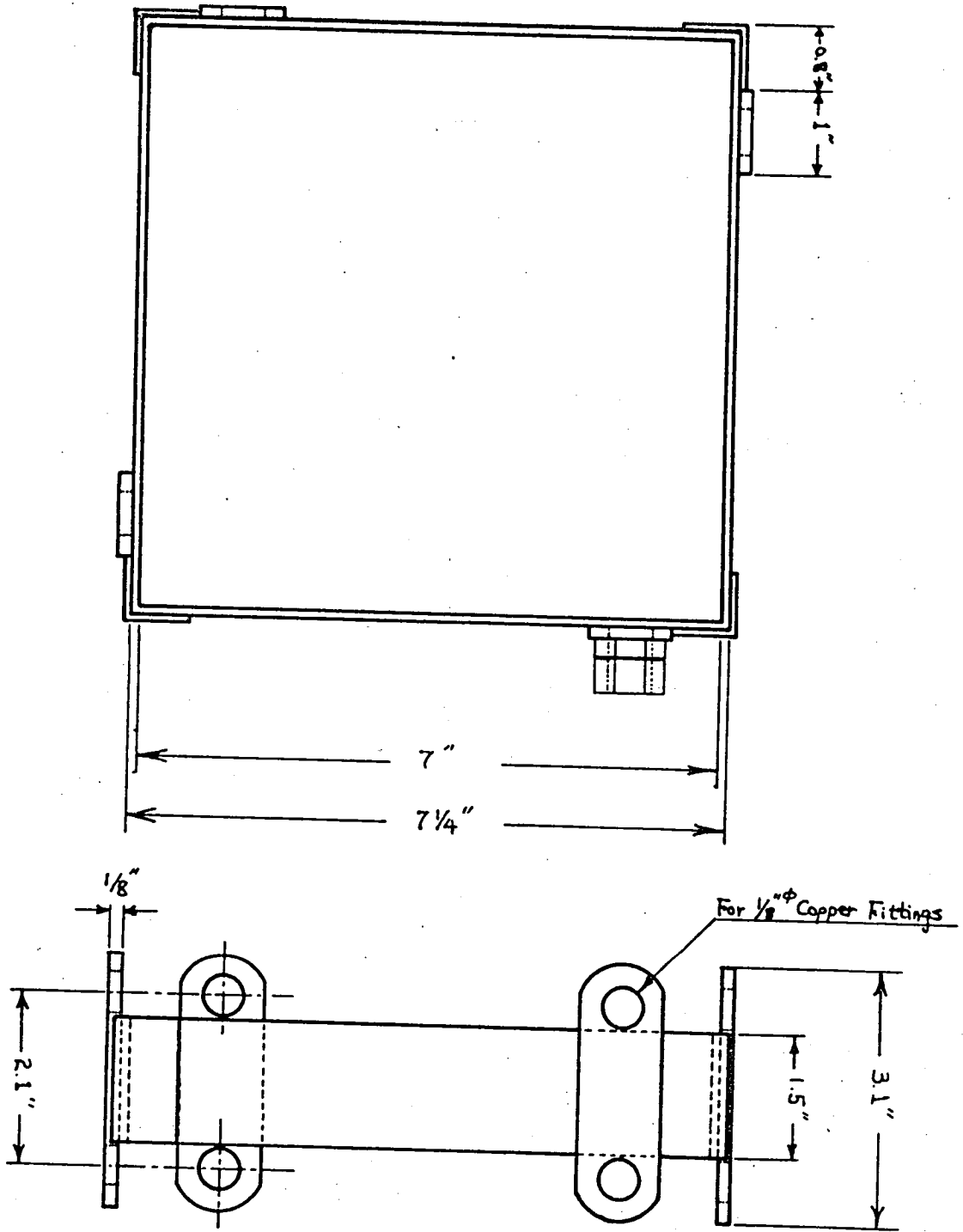


Figure. A-11. Electric Coaxial Cable Connector Frame  
 Material: Brass  
 Scale: 1/2

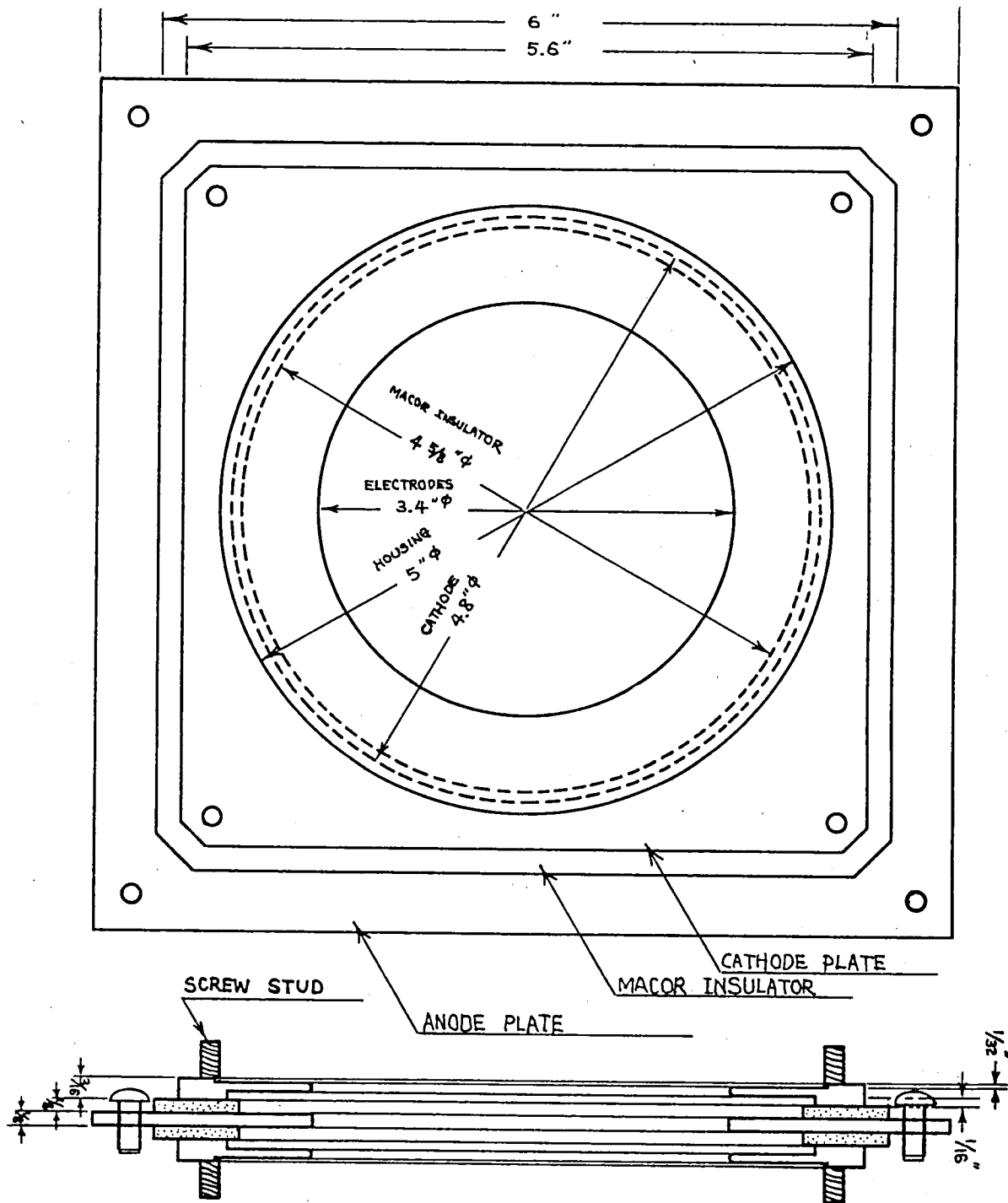


Figure. A-12. Assembly of HCP Plasma Puff Trigger

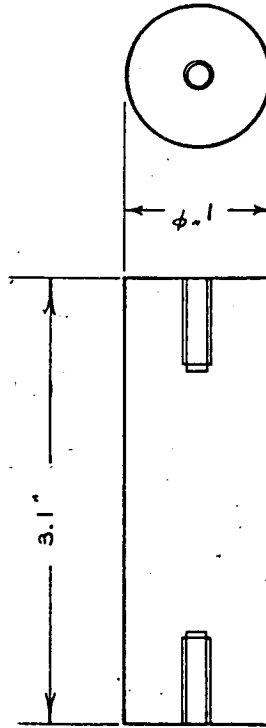


Figure. A-13. Connectors between View Window and Substrate  
Material: Nylon  
Scale: 1/2  
No. of piece: 4 ea.



1. Report No. NASA CR-172420		2. Government Accession No.		3. Recipient's Catalog No.	
4. Title and Subtitle SIMULATION STUDY OF A NEW INVERSE-PINCH HIGH COULOMB TRANSFER SWITCH				5. Report Date October 1984	
				6. Performing Organization Code	
7. Author(s)  SANG H. CHOI				8. Performing Organization Report No. FR 684103	
				10. Work Unit No.	
9. Performing Organization Name and Address INFORMATION & CONTROL SYSTEMS INCORPORATED 28 RESEARCH DRIVE HAMPTON, VA 23666				11. Contract or Grant No. NASA-17488	
				13. Type of Report and Period Covered CONTRACTOR REPORT	
12. Sponsoring Agency Name and Address NATIONAL AERONAUTICS AND SPACE ADMINISTRATION WASHING, DC 20546				14. Sponsoring Agency Code 506-55-73-02	
15. Supplementary Notes Langley Technical Monitor: Nelson W. Jalufka Final Report					
16. Abstract  A simulation study of a simplified model of a new and novel high-coulomb transfer switch has been performed. In contrast to the conventional trigatron switch in which the currents are constricted by the z-pinch mechanism, the new switch operates in an inverse-pinch geometry formed by an all-metal chamber, greatly reducing hot-spot formations on the electrode surfaces. Advantages of the new switch over the conventional switches are longer useful life, higher current capability and lower inductance, which improves the characteristics required for a high repetition rate switch. The simulation study performed here determines the design parameters by analytical computations and comparison with the experimentally measured risetime, current handling capability, electrode damage, and hold-off voltages. Results from the simulation study show that the parameters of initial switch design can be determined for the anticipated switch performance. Results are in agreement with the experiment results. Although the model was simplified, it was accurate enough to determine the switch characteristics such as risetime, current handling capability, electrode damages, and hold-off voltages.					
17. Key Words (Suggested by Author(s)) Inverse-Pinch Mechanism, High Power Switch, Long-Life Switch, High Coulomb Transfer Switch				18. Distribution Statement  Unclassified-Unlimited  Subject Category 33	
19. Security Classif. (of this report) Unclassified		20. Security Classif. (of this page) Unclassified		21. No. of Pages 71	22. Price A04

33

33

LANGLEY RESEARCH CENTER



3 1176 00520 8856

